



OPEN In silico screening of naturally derived dietary compounds as potential butyrylcholinesterase inhibitors for Alzheimer's disease treatment

Md. Tarikul Islam^{1,2}✉, Md. Aktaruzzaman^{2,3}✉, Chandan Barai^{2,4}, Farhan Ishrak Rafi^{2,4}, Al Riyad Hasan^{2,3}, Tasfiah Tasnim^{2,5}, Parvej Sarder^{1,2}, Ghadeer M. Albadrani⁶, Muath Q. Al-Ghadi⁷, Amany A. Sayed⁸, Mohamed M. Abdel-Daim^{9,10}, Humayra Afroz Dona¹¹, Kishore Kumar Sarkar³✉ & Md. Obayed Raihan^{2,12}✉

Alzheimer's disease (AD) is a progressive neurodegenerative condition that causes a substantial decline in cognitive functions and affects memory, thinking abilities, and daily behavior. The most prominent hallmark of AD pathogenesis is the formation of amyloid- β plaques, among other associated pathways such as neurofibrillary tangles, mitochondrial dysfunction, neuroinflammation, and oxidative stress. Butyrylcholinesterase (BuChE), an acetylcholine-degrading enzyme, plays a critical role in the progression of Alzheimer's disease, particularly through its involvement in amyloid- β plaque formation. Thus, the inhibition of BuChE is considered a valuable therapeutic strategy for the management of AD. The present study aimed to identify potential bioactive chemicals from naturally occurring dietary compounds that could improve neurocognitive function and appear as a viable treatment for AD by inhibiting the function of BuChE. A small library of 44 natural dietary chemicals from a variety of dietary plants was subjected to comprehensive in silico studies, including molecular docking, molecular mechanics generalized born surface area (MM-GBSA) calculations, pharmacokinetics assessments, toxicity profiles, molecular dynamics (MD) simulation, and density functional theory (DFT) analysis. These studies revealed that CID 129886986 and CID 115269 showed stronger binding affinities with drug-likeness and no toxicity than the FDA-approved standard drug, Donepezil. Additionally, they exhibited strong structural stability with fewer fluctuations throughout the simulation, making them promising candidates for Alzheimer's disease treatment.

Keywords Alzheimer's disease, Butyrylcholinesterase, Molecular docking, MM-GBSA, Pharmacokinetics, Molecular dynamics simulations, Density functional theory

¹Department of Genetic Engineering and Biotechnology, Faculty of Biological Science and Technology, Jashore University of Science and Technology, Jashore 7408, Bangladesh. ²Laboratory of Advanced Computational Neuroscience, Biological Research on the Brain (BRB), Jashore 7408, Bangladesh. ³Department of Pharmacy, Faculty of Biological Science and Technology, Jashore University of Science and Technology, Jashore 7408, Bangladesh. ⁴Department of Biochemistry and Molecular Biology, Faculty of Science, University of Rajshahi, Rajshahi 6205, Bangladesh. ⁵Department of Mathematics and Natural Sciences, Biotechnology program, BRAC University, Dhaka 1212, Bangladesh. ⁶Department of Biology, College of Science, Princess Nourah bint Abdulrahman University, 84428, 11671 Riyadh, Saudi Arabia. ⁷Department of Zoology, College of Science, King Saud University, P.O. Box 2455, 11451 Riyadh, Saudi Arabia. ⁸Zoology Department, Faculty of Science, Cairo University, Giza 12613, Egypt. ⁹Department of Pharmaceutical Sciences, Pharmacy Program, Batterjee Medical College, P.O. Box 6231, 21442 Jeddah, Saudi Arabia. ¹⁰Pharmacology Department, Faculty of Veterinary Medicine, Suez Canal University, Ismailia 41522, Egypt. ¹¹Department of Genetic Engineering and Biotechnology, Jagannath University, Dhaka 1100, Bangladesh. ¹²Department of Pharmaceutical Sciences, College of Health Sciences and Pharmacy, Chicago State University, Chicago, IL, USA. ✉email: mdtarikulislam448@gmail.com; aktaruzzaman.phar@gmail.com; kk.sarkar@just.edu.bd; mraiha@csu.edu

Abbreviations

AD	Alzheimer's disease
BuChE	Butyrylcholinesterase
MM-GBSA	Molecular mechanics-generalized born surface area
ADME	Absorption, distribution, metabolism, and excretion
SID	Simulation interaction diagram
RMSD	Root mean square deviation
RMSF	Root mean square fluctuation
Rg	Radius of gyration
SASA	Solvent accessible surface area
DFT	Density functional theory

Alzheimer's disease is a progressive, neurodegenerative condition that affects the brain and damages a wide area of the hippocampal region and the cerebral cortex. Most often, abnormalities are first discovered in the frontal and temporal lobes of the brain, and they later spread to other sections of the neocortex at rates that vary significantly from person to person¹. Older people are highly prone to this disease, and prevalence rates are increasing day by day². According to the Alzheimer's Association report 2023, in the past 20 years, with a mortality rate increasing almost 150%, 1 in 3 adults die from Alzheimer's dementia³. Clinically effective treatments are crucial for reducing healthcare costs and improving the quality of life for Alzheimer's patients⁴. There are numerous hypotheses regarding the preliminary cause of AD, including cholinergic neuron damage, the aggregation of proteins such as amyloid- β ($A\beta$) in plaques, hyperphosphorylated-tau in neurofibrillary tangles leading to significant loss of synapses, inflammation, and oxidative stress⁵. According to the $A\beta$ hypothesis, the accumulation of $A\beta$ deposits is a key factor in Alzheimer's disease (AD), leading to the formation of neurofibrillary tangles, neuronal death, vascular damage, and dementia. $A\beta$ peptides are generated by the abnormal cleavage of amyloid precursor protein (APP) by secretases⁶. The β -site APP cleavage enzyme (BACE) cuts APP to release the sAPP β fragment, leaving the CTF99/89 fragment. This fragment is further cleaved by γ -secretase to produce $A\beta$ peptides, with $A\beta$ 40 and $A\beta$ 42 being the most prevalent forms⁷. In addition to $A\beta$ plaques, the formation of neurofibrillary tangles (NFTs) composed of abnormal tau protein aggregates is another key hallmark. Tau, a protein associated with microtubules, is crucial for maintaining the stability of neuronal microtubules and supporting cellular functions⁸. In healthy neurons, tau is properly regulated and phosphorylated, allowing it to bind to microtubules and facilitate their assembly⁸. However, in AD, tau undergoes abnormal changes, such as hyperphosphorylation, which impairs its normal function⁹.

In the cholinergic hypothesis of AD, the dysfunction of acetylcholine (ACh) is a central feature. BuChE, an enzyme similar to acetylcholinesterase (AChE), breaks down ACh in the brain¹⁰. In AD, BuChE levels increase as a compensatory mechanism for the loss of AChE activity. This increased BuChE activity further contributes to the breakdown of ACh, exacerbating cholinergic dysfunction and cognitive decline¹¹.

Some investigations demonstrated that BuChE activity increases (40–90%) in the most affected areas of the brain, such as the temporal cortex and the hippocampus, during the development of AD¹². Therefore, inhibition of BuChE has been identified as a crucial AD therapeutic target to increase the availability of acetylcholine (ACh) in the brain regions and decrease the $A\beta$ deposition¹³. BuChE is most frequently linked with plaques, which are fibrillar amyloid-pleated sheets of $A\beta$ form¹⁴. In other words, BuChE activity linked with $A\beta$ plaques appears to be a characteristic that separates AD disease from plaques seen in the brains of people who do not have dementia. According to several studies, when BuChE gets linked with plaques, it promotes the change of “benign” plaques into “malignant” plaques that are diagnostic of AD¹⁵. However, the current FDA-approved cholinesterase inhibitors (Rivastigmine, Galantamine, Tacrine, and Donepezil) do not selectively target BuChE, and their efficacy is limited¹³. Furthermore, Tacrine manufacture was halted in 2013 owing to hepatotoxicity, restricting the options for treating Alzheimer's disease¹⁶. Given the limitations of existing treatments, especially the side effects and the complexity of AD, dietary plants have gained attention as a source of naturally occurring drug-like molecules for AD treatment. Recent studies have shown that certain dietary plant compounds may alleviate neurodegenerative conditions, making them a promising area of research.^{17–19}

Conventional drug development approaches include finding and validating targets, finding and optimizing lead molecules, and running preclinical and clinical trials, which are very expensive and time-consuming. To reduce costs and development time, computer-aided drug design (CADD) offers powerful tools and techniques to assist in various stages of drug discovery.²⁰ This study aims to identify potential BuChE inhibitors as drug candidates for AD treatment by utilizing a CADD approach focused on dietary plant ingredients.

Materials and methods

Identification of dietary chemicals through literature review

Dietary bioactive compounds are natural food substances that support health by modulating biological activities and essential physiological functions, helping reduce the risk of chronic diseases like cardiovascular conditions, cancer, and neurodegenerative disorders²¹. A total of 44 dietary compounds were collected based on the ethno-medicinal use and anti-inflammatory activities of the compounds, along with their source dietary plants, through literature review, as shown in Supplementary Information (SI) 1.

Protein structure retrieval and preparation

The crystal structure of human Butyryl cholinesterase protein (PDB ID: 1P0I) was retrieved from the RCSB Protein Data Bank (<https://www.rcsb.org/>) (Fig. 1)²². The amino acid sequence length of human Butyryl cholinesterase protein is 529, with a resolution of 2.00 Å. The Schrodinger Protein Preparation Wizard was used

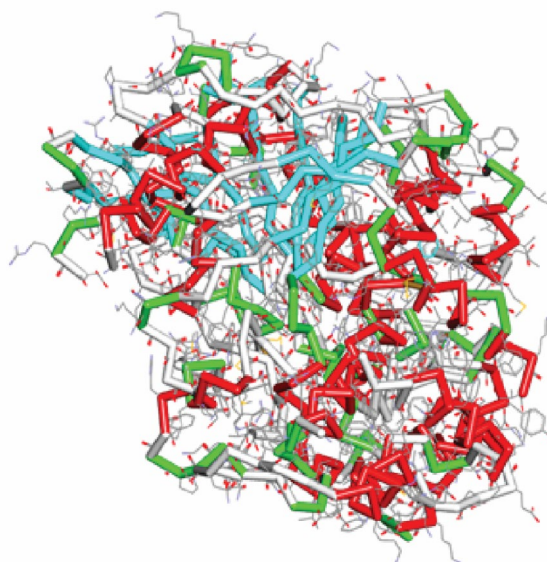


Fig. 1. The 3D X-ray crystal structure of human butyryl cholinesterase protein (PDB ID: 1P0I).

to optimize the protein structure by adding hydrogen atoms, replacing missing residues, and fixing the formal charges on the hetero groups^{23,24}. Then the protein structures were optimized with the OPLS3 force field²⁵.

Compounds retrieval and preparation

An amount of 44 dietary chemicals along with the control drug (donepezil) were downloaded from the PubChem database (<http://www.ncbi.nlm.nih.gov/pcc/chem>) in 2D and 3D SDF format. Then, the ligands were prepared for molecular docking through refinement and processing using the LigPrep module in Maestro v11.3^{26,27}. Finally, the LigPrep v-55139 was used for preparing ligands²⁸. Finally, the docking analysis was optimized using the OPLS3 force field²⁵.

Molecular docking analysis

Molecular docking is a computational method used to calculate the binding energies of small molecules with target receptors^{26,29,30}. The binding energy of target protein–ligand complexes was evaluated through molecular docking analysis³¹. The FTSite server (<https://ftsites.bu.edu/>) was utilized in this study to map the protein's active site and generate a receptor grid for assessing the binding affinity of the chemicals³². A grid box with dimensions of X = 7.25, Y = 2.53, and Z = 33.1 was generated for 1P0I to define the area for small-molecule docking modeling. In this analysis, molecular docking studies on a screen of compounds were conducted using the Glide package v-8.8 and Maestro v-12.5.139 from the Schrödinger Suite. For docking, the OPLS3 force field was used in standard precision (SP) mode to minimize the systems²⁵.

MM-GBSA analysis

MMGBSA (Molecular Mechanics/Generalized Born Surface Area) analysis is a computational method for estimating the binding free energy of a ligand–protein complex by integrating molecular mechanics energies with solvation effects to predict stability and affinity^{33,34}. The prime MMGBSA program package was used to predict the MM-GBSA score using the novel energy solvation model, VSGB. This analysis evaluates the binding free energies of the control compound and the identified ligands in relation to the selected receptor. The negative MM-GBSA ΔG bind values for NS, Coulomb energy (ΔG bind Coulomb), hydrogen bond energy (ΔG bind H-bond), lipophilicity energy (ΔG bind lipo), and van der Waals interaction energy (ΔG bind vdW) were taken into account for this analysis. These energy contributions offer insights into the ligand, receptor, and complex structures, along with energy differences associated with strain and binding.

Pharmacokinetics and toxicity analysis

The computer-aided drug design and development process includes a crucial assessment of ADME/T (absorption, distribution, metabolism, excretion, and toxicity) to identify molecules with optimal pharmacokinetic properties, ultimately leading to the discovery of effective drugs³⁵. The SwissADME server (<http://www.swissadme.ch/>), a free web tool, was used in this study to assess the initial pharmacokinetic properties of the compounds³⁶. Toxicity analysis evaluates the extent to which a substance harms an organism or its substructures, such as cells or tissues, and is a crucial step in drug development. Therefore, we evaluated the toxicity of the selected compounds using the ProTox-3.0 server (<https://tox.charite.de/protox3/>)³⁷.

Molecular dynamics (MD) simulation analysis of protein–ligand complexes

MD simulation is an essential technique for observing conformational changes, enabling ligand–receptor complexes to evolve over a specific time scale in an artificial environment^{33,38,39}. A 250 ns MD simulation was considered to assess the stability of the complexes formed by our selected candidate compounds, focusing on their binding to the active site of the target protein using the 'Desmond v3.6 Program' in Schrodinger (Academic version) on a Linux platform⁴⁰. To maintain a specified volume, the TIP3P water model was utilized, and an orthorhombic periodic boundary box with a 10 Å distance on both sides was created. To neutralize the system, Na⁺ and Cl[−] were added to reach a molar salt concentration of 0.15 M. After constructing the solvated system including the protein–ligand complex, the system minimization and relaxation using the Desmond module's default protocol, with OPLS3 force field settings, were used²⁵. The Nose–Hoover temperature coupling and isotropic scaling approach were employed, with energy collected at 100 ps intervals, to maintain the NPT ensembles at 310 K and 1.01325 bar of atmospheric pressure.⁴¹ Using a variety of metrics, such as the root-mean-square deviation (RMSD), root-mean-square fluctuation (RMSF), radius of gyration (Rg), and solvent-accessible surface area (SASA), we evaluated the stability of protein–ligand complexes over the 250 ns trajectory. The Desmond module's v6.3 simulation interaction diagram (SID) was used for these evaluations.

RMSD analysis

RMSD provides an assessment of the average positional displacement of atoms, typically remarking on the deviation of the backbone or heavy atoms in comparison to their native state over the runtime of the simulation³⁴. RMSD analysis was used to anticipate the structural integrity of the protein–ligand complex within a hydrated environment by quantifying the deviation between two atomic coordinates⁴². For each protein–ligand complex, the RMSD analysis data of the whole simulation duration (250 ns) was calculated using the following equation:

$$RMSDx = \sqrt{\frac{1}{N} \sum_{i=1}^N (r'_i(t_x)) - (r_i(t_{ref}))^2}$$

In this equation,

N = The number of selected atoms, t_{ref} = The reference or specified time.

r = The specified atom's location in the frame, t_x = The duration of the recording intervals.

RMSF analysis

RMSF analysis assesses the residue-specific flexibility of a ligand-bound protein by measuring changes in mean residue positions, providing insights into structural and conformational shifts over time in a simulation model⁴³. The RMSF analysis results were derived from the following equation for each protein residue throughout the simulation:

$$RMSFx = \sqrt{\frac{1}{T} \sum_{t=1}^T \langle (r'_i(t)) - (r_i(t_{ref}))^2 \rangle}$$

In this equation,

T = Trajectory time, t_{ref} = Reference time, r = The selected atoms' position in the frame, $\langle \rangle$ = The average square distance traveled over residues.

Rg Analysis

The radius of gyration (Rg) calculates the mass-weighted average distance of atoms from the center of mass in a ligand-bound protein complex, assessing the compactness of ligand–macromolecule complexes during the simulation⁴⁴. The Rg values were calculated using the following equation to carry out the Rg analysis for the 250 ns simulation:

$$Rg = \sqrt{\frac{1}{N} \sum_{i=1}^N |r(i) - r_{center}|^2}$$

In this equation,

N = The number of protein atoms, r(i) = The coordinates of a specific atom, r_{center} = Center of mass.

SASA analysis

SASA analysis examines protein folding, hydrophilic and hydrophobic interactions, and binding site accessibility by measuring the exposed surface area of protein–ligand complexes in the solvent. It was used throughout the simulation to assess ligand incorporation and complex stability⁴⁵. It also describes the folding–unfolding pattern of the protein–ligand complex. The change in solvent contact area during the simulation was quantified and analyzed to provide insights into the packing nature of the complex⁴⁶.

DFT analysis

The density function theory (DFT) was conducted using B3LYP in conjunction with a 6-31G⁴⁷ basis set⁴⁸ to gain insights into the quantum chemical characteristics of the compounds of interest. The Gaussian 09W software package was used to compute various quantum mechanical properties. Mainly, the frontier orbital study was conducted as the energy gap between the highest occupied molecular orbital (HOMO) and the lowest unoccupied molecular orbital (LUMO) of a compound defines its reactivity⁴⁹. Additionally, reactivity descriptors such as ionization potential, electron affinity, electronegativity (χ), electronic potential (μ), chemical hardness (η), electrophilicity (ω), and chemical softness (σ) were assessed using the DFT approach. The energy gap was calculated using the following equation:

$$\Delta E = E_{LUMO} - E_{HOMO}$$

Koopmans' theorem was utilized to project a relationship between a compound's structural and electric characteristics.

Principal component analysis

PCA is a commonly used statistics-dependent analysis technique to identify the predominate coordinated motions of the protein domains during dynamic simulation. The principal components' direction and their significance in explaining the variance in the data are shown by eigenvectors, which also serve as the foundation for PCA⁵⁰. Principal components (PCs) corresponding to the largest eigenvalues, represent most of the variance of the system, pointing out the important coordinated motions⁵¹. The PCA approach has been significant in revealing large-scale conformation changes that might affect the inhibitory mechanism. The PCA analysis was performed using R version 4.4.0 along with the Bio3D package.

Free energy landscape (FEL) analysis

FEL was carried out to understand the conformational change for achieving stability of the protein–ligand complex and displayed via an energy map. The FEL of each complex was plotted following the projection of its first two principal components (PC1 and PC2) or eigenvectors⁵². Calculations with Boltzmann distribution were applied to determine free energy, and the most conformations correspond to the least energy associated with the favorable binding of the ligand, which increases its inhibitory activity⁵³. The PCA analysis was conducted using R version 4.4.0 along with the Bio3D package. PCA analysis on the simulation trajectories was done utilizing the following equation:

$$\Delta G(PC1, PC2) = -K_B T \ln P(PC1, PC2)$$

In this equation,

K_B = The Boltzmann constant, PC1, PC2 = Dominant fluctuation,

$P(PC1, PC2)$ = Probability distribution of the first two principal components of the system.

DCCM analysis

The cross-correlation matrix study was applied to gain a 3D understanding of the comparative conformational motion of protein residues over time. DCCM (Dynamic Cross-Correlation Matrix) calculations are based on the covariance of atomic displacements, providing insights into residue movements and their correlations. Positive correlation values indicate residues moving in concert, while negative values signify anti-correlated motions⁵⁴. The trajectories drawn from the simulation determined the correlation motion between docked complex residues⁵⁵. This analysis allowed the description of the structural regions involved in ligand binding and the global protein motions. The DCCM analysis was calculated using the following equation:

$$C_{ij} = \frac{(\Delta R_i \cdot \Delta R_j)}{\sqrt{(\Delta R_i \cdot \Delta R_i)(\Delta R_j \cdot \Delta R_j)}}$$

In this equation,

$\Delta R_i, \Delta R_j$ = Displacement of i th and j th atom from the mean, C_{ij} = The coefficient of cross-correlation.

Results

Interpretation of molecular docking analysis

Molecular docking is a widely used bioinformatics-based method used to make assumptions about the possible interaction between ligands and a protein complex via a computer platform. It helps predict the binding affinity between two molecules and predicts the best binding pose of the molecules based on the lowest binding energy⁵⁶.

In this study, the top three compounds, CID 115269, CID 445154, and CID 129886986, were identified based on their better binding affinities with the protein target BuChE among 44 chemicals, as shown in supplementary information (SI) 2. Donepezil (CID 3152) was used as a standard drug molecule to compare the competency of the compounds of our interest. The Glide docking score for CID 3152, standard donepezil with BuChE, was observed at -8.28 kcal/mole (Table 1). Our compounds of interest, CID 115269, CID 445154, and CID 129886986 with BuChE, exhibited docking scores of -10.37 , -10.61 , and -11.88 kcal/mole (Table 1).

Interpretation of 2D, and 3D binding interactions of molecular docking studies

The visualization of the 2D and 3D interactions of the control compound and identified ligands with the target protein was conducted through the Schrodinger Suite. The analysis unveiled the site-specific hydrogen

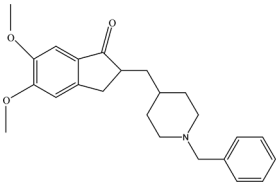
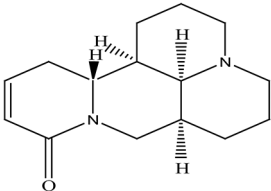
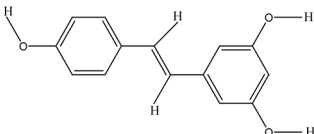
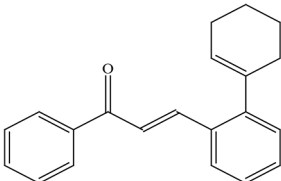
SN	PubChem ID	Phytochemical name with 2D structure	Binding affinity (kcal/mol)
01	CID 3152	 Donepezil (C ₂₄ H ₂₉ NO ₃)	-8.28
02	CID 115269	 Sophocarpine (C ₁₅ H ₂₂ N ₂ O)	-10.37
03	CID 445154	 Resveratrol (C ₁₄ H ₁₂ O ₃)	-10.61
04	CID 129886986	 Cyclohexenyl chalcone (C ₂₁ H ₂₀ O)	-11.88

Table 1. Molecular docking scores of the identified three compounds along with the control compound.

bonds, hydrophilic bonds, and other bonds during stable ligand-target, control-target interactions. Our control compound, CID 3152, exhibited one hydrogen bond interaction with the GLH197 residue, five hydrophilic bond interactions with SER79, GLN119, THR120, SER198, and SER287 residues, and other bonds were observed at ASP70, TRP82, TYR114, GLY115, GLY116, GLY117, GLY121, TYP128, PRO285, LEU286, VAL288, ALA328, PHE329, TYR332, TRP430, HIP438, GLY439, and ILE442 residues (Table 2 and Fig. 2). CID 115269 formed H-bond in the same GLH197 residue as CID 3152; it also showed two ionic bonds at SER79 and THR120 residues and several other interactions at ASP70, GLY78, TRP82, GLY115, GLY116, GLY121, TYR129, ALA328, PHE329, TYR332, TRP430, MET437, HIP438, GLY439, TYR440, and ILE442 residues of the 1P0I protein. Although CID 445154 exhibited two hydrogen bonds at THR120 and ALA328 residues, CID 129886986 didn't participate in any H-bond formation. Polar interaction counted for CID 445154 is one and at the same THR120 residue, where it formed H-bonds with protein, but counts for CID 129886986 are four and at SER79, GLN119, THR120, and SER287 residues. Along with the H-bonds and hydrophilic bonds or polar interactions, some other interactions were observed. These other interactions like covalent interactions, and pi-pi stacking interactions for CID 445154 were found at GLY78, TRP82, TYR114, GLY115, GLY116, GLY121, LEU125, TYR128, GLH197, PHE329, VAL331, TYR332, TRP430, MET434, MET437, HIP438, GLY439, TYR440, and ILE442 residues and for CID 129886986 were observed at ASP70, TRP82, GLY115, GLY116, GLY117, TYR128, GLH197, PRO285, LEU286, ALA328, PHE329, TYR332, TRP430, HIP438, GLY439, and ILE442 residues.

Protein	Phytochemical (PubChem) ID	H-bonds	Hydrophilic bonds	Other bonds
1P0I	CID 3152	GLH197	SER79, GLN119, THR120, SER198, SER287	ASP70, TRP82, TYR114, GLY115, GLY116, GLY117, GLY121, TYR128, PRO285, LEU286, VAL288, ALA328, PHE329, TYR332, TRP430, HIP438, GLY439, ILE442
	CID 115269	GLH197	SER79, THR120	ASP70, GLY78, TRP82, GLY115, GLY116, GLY121, TYR129, ALA328, PHE329, TYR332, TRP430, MET437, HIP438, GLY439, TYR440, ILE442
	CID 445154	THR120, ALA328	THR120	GLY78, TRP82, TYR114, GLY115, GLY116, GLY121, LEU125, TYR128, GLH197, PHE329, VAL331, TYR332, TRP430, MET434, MET437, HIP438, GLY439, TYR440, ILE442
	CID 129886986		SER79, GLN119, THR120, SER287	ASP70, TRP82, GLY115, GLY116, GLY117, TYR128, GLH197, PRO285, LEU286, ALA328, PHE329, TYR332, TRP430, HIP438, GLY439, ILE442

Table 2. Interactions of amino acid residues with the identified ligands, along with the control compound, with the targeted receptor.

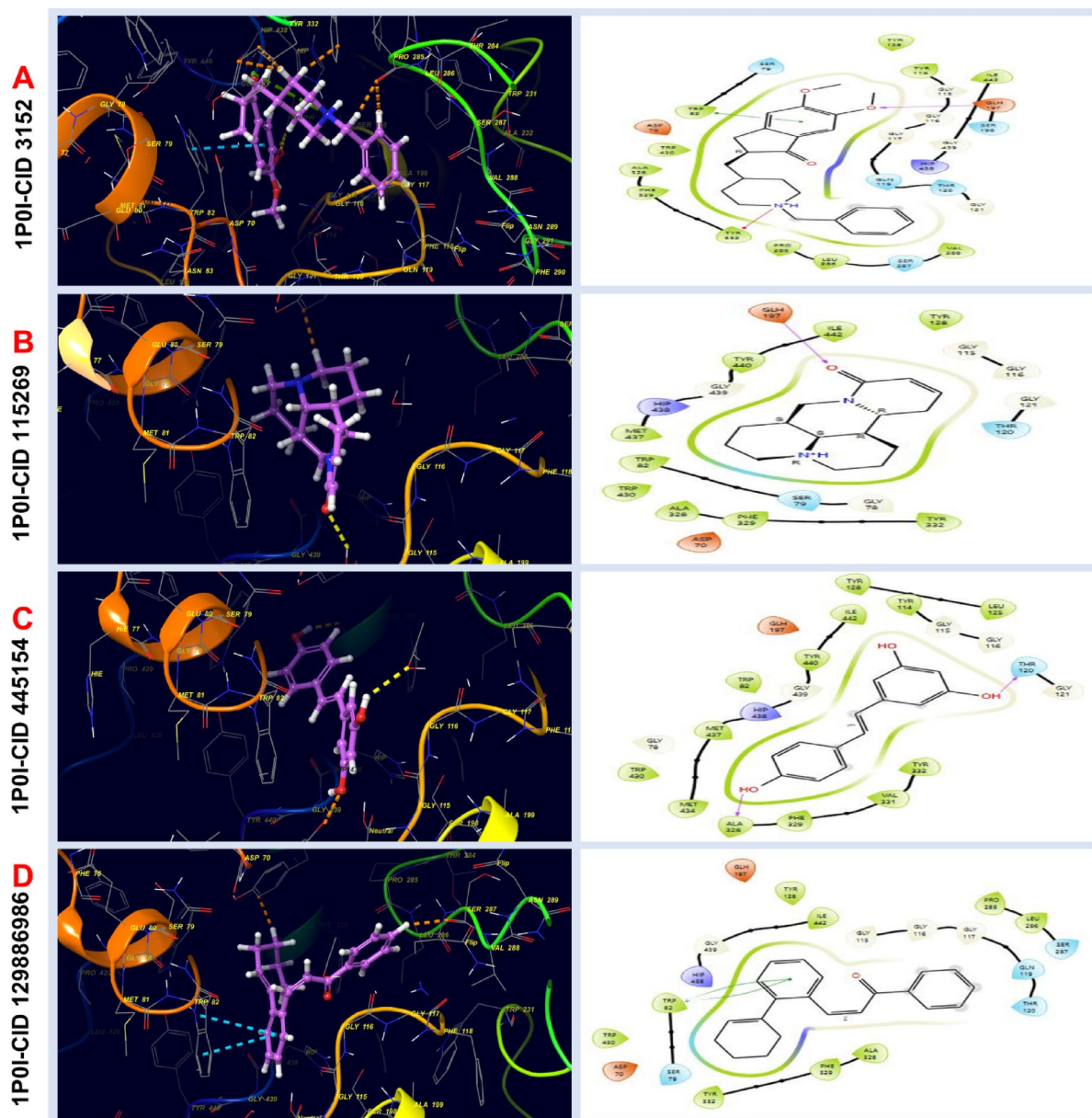


Fig. 2. Molecular docking configurations and interactions with 1P0I protein. The complexes of protein–ligand interactions in 2D are presented on the right side, while the 3D observations are shown on the left. (A) CID 3152; (B) CID 115269; (C) CID 445154; and (D) CID 129886986.

MM/GBSA analysis

MM-GBSA evaluates the binding free energy between a drug molecule and its target protein, offering detailed molecular insights into the stability and strength of the protein–ligand complex. Our findings demonstrated notable binding affinities, as evidenced by the ΔG values, which highlight strong interactions between the candidate ligands and the target protein, as shown in Fig. 3. The MM-GBSA analysis of the top three chemicals, CID 445154, CID 115269, and CID 129886986, revealed higher binding free energies with the 1P0I protein, calculated at -41.03 , -49.99 , and -46.53 kcal/mol, respectively, in comparison to the control compound's binding energy of -29.06 kcal/mol.

Pharmacokinetic properties and toxicity analysis

ADME analysis was done to assess the drug-likeness of the top two compounds: CID 115269 and CID 129886986. The standard drug molecule CID 3152 was also subjected to ADME analysis to better evaluate the pharmacokinetic properties of the top compounds. Moreover, toxicity analysis was performed to assess toxicological effects on biological systems and to have an idea of possible lethal doses of each compound. In this study, ADME analysis was performed by using the SwissADME web server, and toxicity analysis was performed using the ProTox 3.0 web server, as presented in Table 3.

Drug likeliness properties were checked as per Lipinski's rule of five. Compounds that showed better pharmacokinetic properties and follow Lipinski's rule of five are considered better drug candidates⁵⁷. Only CID 129886986 violated one rule among all three compounds. According to Lipinski's rule of five, a drug or drug-like molecule should have a Log Po/w(MLOGP) value of less than or equal to 4.15. A higher Log Po/w(MLOGP) indicates a higher lipophilicity. CID 129886986 has a slightly higher Log Po/w(MLOGP) value of 4.38, suggesting higher lipophilicity than CID 3152 and CID 115269. All three compounds showed high GI absorption properties and BBB permeability, indicating better pharmacokinetic properties.

In toxicity analysis, CID 3152 exhibited a higher probability of neurotoxicity along with higher immunotoxicity and cytotoxicity than our interest compounds. As per the LD50 value, CID 129886986 has the highest value of 1048 mg/kg, suggesting it is less toxic than the other two compounds and is consumable at higher doses. Both CID 115269 and CID 129886986 showed fewer toxic effects than the standard drug molecule and showed great pharmacokinetic properties during analysis, making them considerable drug candidates.

MD simulation

MD simulation analysis is a simulation method performed to determine the stability of the ligand-macromolecule complex in an artificial environment. This method calculates the ligand-macromolecule complex interaction and energy changes by solving the laws of thermodynamics⁵⁸. A 250 ns MD simulation was conducted on the Schrodinger platform to realize the binding interaction, flexibility, and stability of compounds CID 129886986 and CID 115269 in the protein–ligand complexes. CID 3152 (donepezil) was considered as a standard ligand, and the protein BuChE (1P0I) was the target to compare the results of the compounds of interest.

RMSD analysis

To assess the stability of ligand-macromolecule complexes in a hydrated environment, their movements were analyzed by plotting root mean square deviation (RMSD) values over time⁵⁹. The RMSD values of protein backbone atoms construct a clear view of the equilibrium and stabilization of MD trajectories. Higher overall RMSD scores indicate a loss of conformational integrity, whereas lower values suggest greater structural

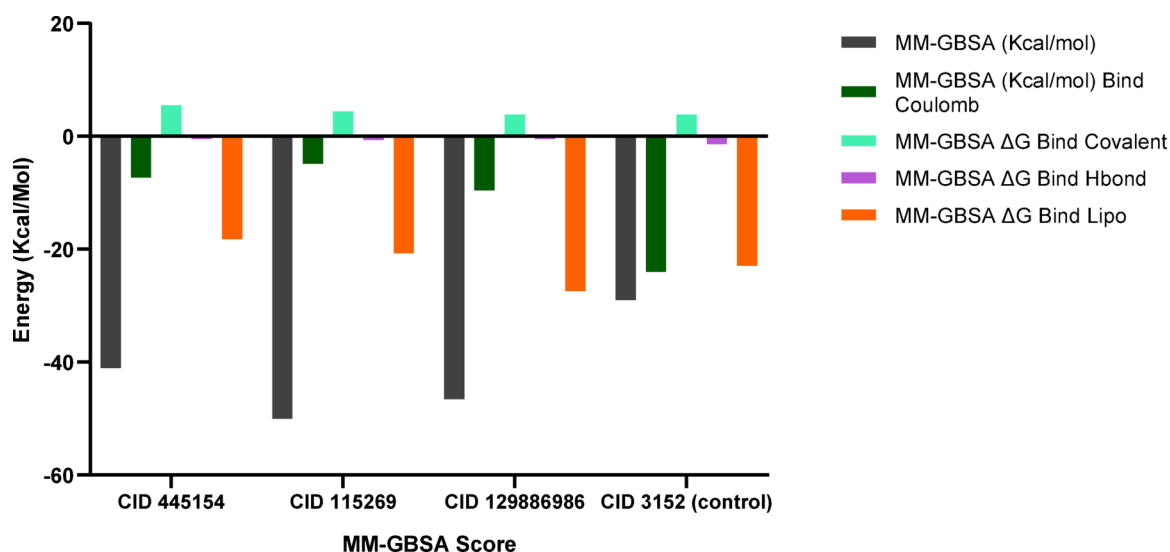


Fig. 3. Illustrating the MM-GBSA analysis results for compounds CID 445154, CID 115269, and CID 129886986, and the control compound CID 3152, examining their binding interactions with the target receptor 1P0I.

Phytochemical identifier		CID 3152	CID 115269	CID 129886986
Pharmacokinetics properties	MW (g/mol)	379.49 g/mol	246.35 g/mol	288.38 g/mol
	Heavy atoms	28	18	22
	Arom. heavy atoms	12	0	12
	Rotatable bonds	6	0	4
	H-bond acceptors	4	2	1
	H-bond donors	0	0	0
	Log Po/w(MLOGP)	3.06	2.16	4.38
	Log S (ESOL)	− 4.81	− 2.45	− 5.18
	GI absorption	High	High	High
	Lipinski, Violation	0 violation	0 violation	1 violation
	Synth. Accessibility	3.36	4.38	3.26
	BBB permeant	Yes	Yes	Yes
Toxicity	Neurotoxicity (Probability)	Active (0.9)	Active (0.67)	Active (0.66)
	Hepatotoxicity (Probability)	Inactive	Inactive	Inactive
	Carcinogenicity (Probability)	Active (0.5)	Inactive	Inactive
	Immunotoxicity (Probability)	Active (0.95)	Inactive	Active (0.61)
	Mutagenicity (Probability)	Inactive	Inactive	Inactive
	Cytotoxicity (Probability)	Active (0.53)	Inactive	Inactive
	LD50	505 mg/kg	196 mg/kg	1048 mg/kg

Table 3. Pharmacokinetic properties and toxicity analysis of the selected drug molecules.

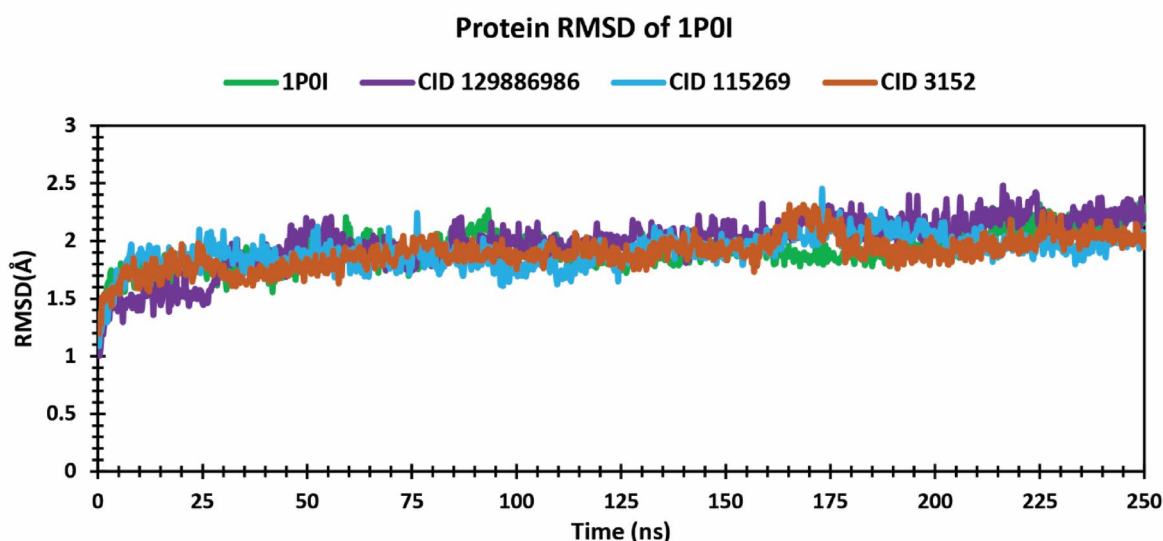


Fig. 4. RMSD values of the docked protein–ligand complexes over a 250-ns simulation time. The colors orange, blue, and purple, respectively, represented docked protein with the three compounds CID 3152, CID 115269, and CID 129886986, while green represented apo-protein.

stability³³. In our studies, the protein with all three compounds in the protein–ligand complexes and the apo-protein showed no massive fluctuations, indicating higher structural stability of the complexes. The average RMSD values of the apo-protein (BuChE) as well as of protein (1P0I) in complex with CID 129886986, CID 115269, and CID 3152, calculated, were 1.92 Å, 1.99 Å, 1.91 Å, and 1.9 Å, respectively (Fig. 4). The protein exhibited almost overlapping RMSD values in complexes with both of our identified compounds as the unbound BuChE protein. Between our identified compounds, CID 115269 in complex with 1P0I had the lowest value, indicating it possesses the most stable conformation. Protein (1P0I) in the complex with CID 115269 showed the most similar trajectories with apo-BuChE compared to CID 129886986. The protein–ligand complexes exhibited increasing RMSD values from 0 to 10 ns before stabilizing. However, CID 129886986 showed a sudden RMSD rise between 25 and 35 ns before regaining stability. During simulation, the protein complexed with CID 129886986 and CID 115269, along with standard CID 3152, showed minor fluctuations around the 160 to 200 ns timeframe compared to the apo-protein. The RMSD trajectories indicated that 1P0I in complexes with

CID 129886986 and CID 115269 maintained structural integrity throughout the simulation, with no significant deviations from their initial configurations.

RMSD analysis of ligand in complex with protein

The RMSD analysis of the ligands in the complex with the protein was conducted to get a clearer insight into the binding stability within the complex. The RMSD trajectory deviations ranging up to 3 Å are considered the acceptable range for the stability of the ligand in a biological system. A deviation higher than this limit indicates a conformational change within the structure³¹. The standard ligand CID 3152 in complex with the 1P0I protein exhibited the highest average RMSD value of 3.02 Å, showing significant fluctuations compared to other identified compounds over 250 simulation runs. Both ligands, CID 129886986 and CID 115269, in the protein–ligand complex, showed a lower average RMSD value of 1.02 Å and 0.22 Å, respectively, than the standard CID 3152. From 0 to 174 ns, the RMSD values of CID 129886986 in complex with the 1P0I protein ranged from 0.41 Å to 1.36 Å, maintaining a stable pattern with no significant fluctuations. However, a sudden rise to 2.19 Å was observed until 180 ns, suggesting a possible conformational change. After 180 ns, the complex stabilized, exhibiting no significant structural shifts. Whereas, in complex with 1P0I protein, ligand CID 115269 showed no major fluctuations throughout the entire simulation, exhibiting a highest peak of 0.89 Å at 9 ns. CID 115269 in complex with 1P0I protein exhibited the most stability in comparison to all the other ligands (Fig. 5).

RMSF analysis

To better understand the conformational stability and structural flexibility of Ca atoms in every compound in the corresponding system, root mean square fluctuations (RMSF) data were analyzed³¹. According to Fig. 6, RMSF data from a 250 ns MD simulation showed that CID 129886986, CID 115269, and CID 3152 in complex with the 1P0I protein exhibited similar flexibility, closely aligning with the protein's trajectory behavior. For apo-protein, it showed some minor fluctuations for Ca atoms around PRO74, TRP 376, GLU411, HIS428, and ARG453 amino acid residues at 71, 373,406,423, and 448 positions. CID 3152 in complex with 1P0I protein exhibited fluctuations for Ca atoms around GLN71, VAL377, ARG453, and SER487 residues at 68, 374, 448, and 481 positions. In complexes with 1P0I protein, CID 129886986 and CID 115269 both showed a peaks at 374 and 448 positions like CID 3152. Apart from that, CID 129886986 in complex with 1P0I protein depicted two peaks for Ca atoms around VAL72 and THR483 amino acid residues at positions 69 and 477, respectively, suggesting no significant fluctuations over the simulation period. Also, CID 115269 in complex with 1P0I protein showed a peak for Ca atoms around VAL280 amino acid residue at position 277. The overall trajectories exhibited the highest peaks at the N and C terminal domains, reflecting the lower chance of dissociation of compounds of our interest from the biological model of the protein–ligand complex.

Rg analysis

The radius of gyration (Rg) values of the compounds in complex with protein were plotted against simulation time to understand the compactness of the protein–ligand structure. The Rg value is inversely proportional to the compactness of the protein–ligand complex, and for firmly folded protein states, the value remains stable⁶⁰. In 250 ns simulation time, the standard CID 3152 in complex with 1P0I protein exhibited an increased Rg value from 115 to 175 ns, suggesting the most compactness with BuChE protein, having an average Rg value of 3.02 Å,

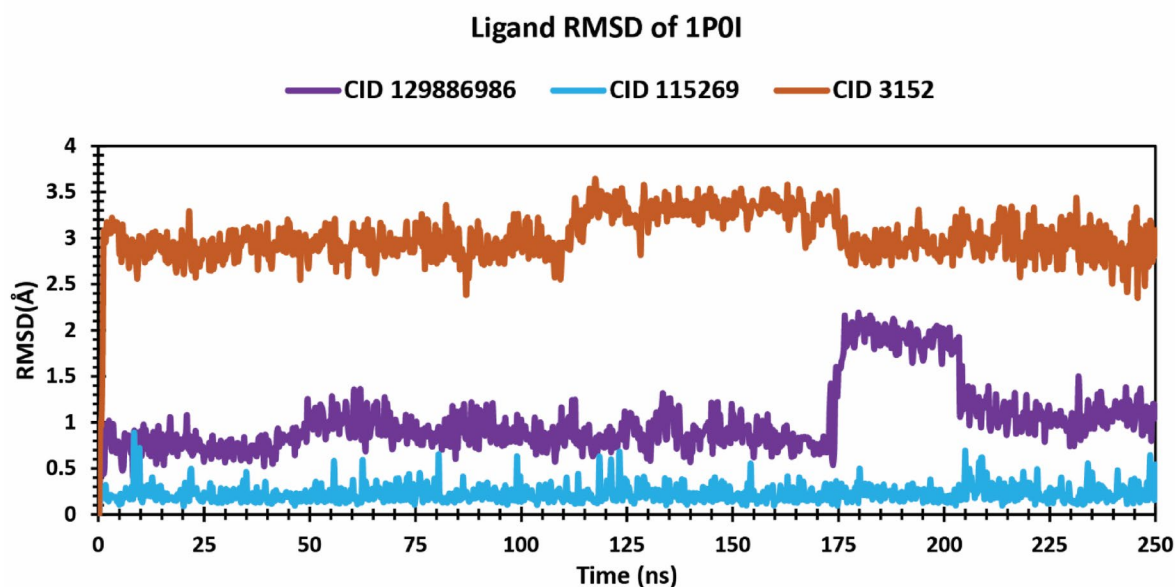


Fig. 5. RMSD values of the docked ligands over 250 simulation run time. The colors orange, blue, and purple were used to represent the compounds CID 3152, CID 115269, and CID 129886986, respectively.

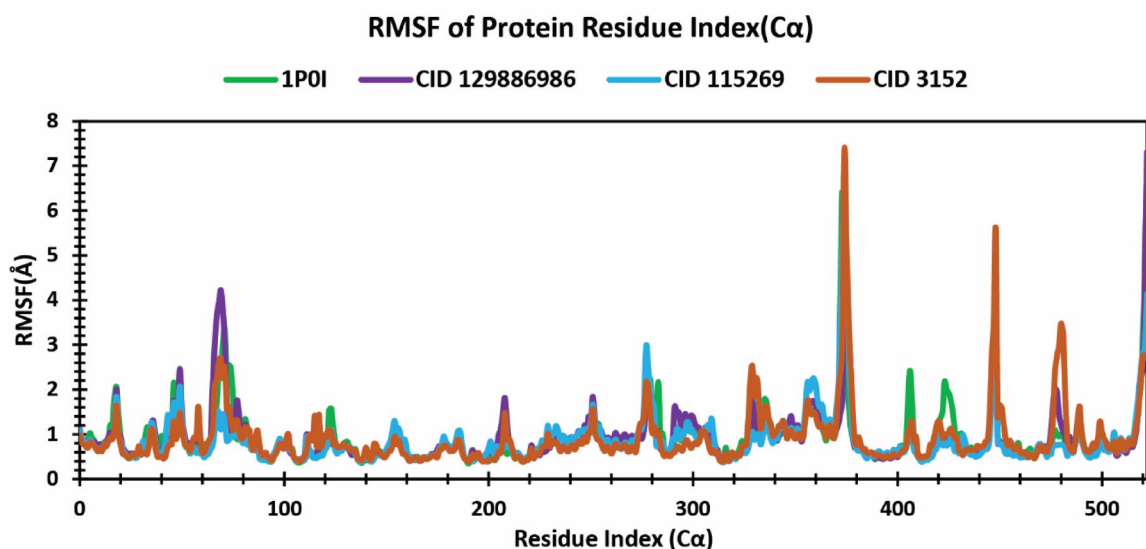


Fig. 6. RMSF analysis of the residues of amino acids during a 250 ns simulation period. The protein Cα atoms in the protein–ligand complexes were used to calculate the RMSF values. Green represents Apo-protein 1P0I, whereas orange, blue, and purple represent the three complexes bound to CID 3152, CID 115269, and CID 129886986, respectively.

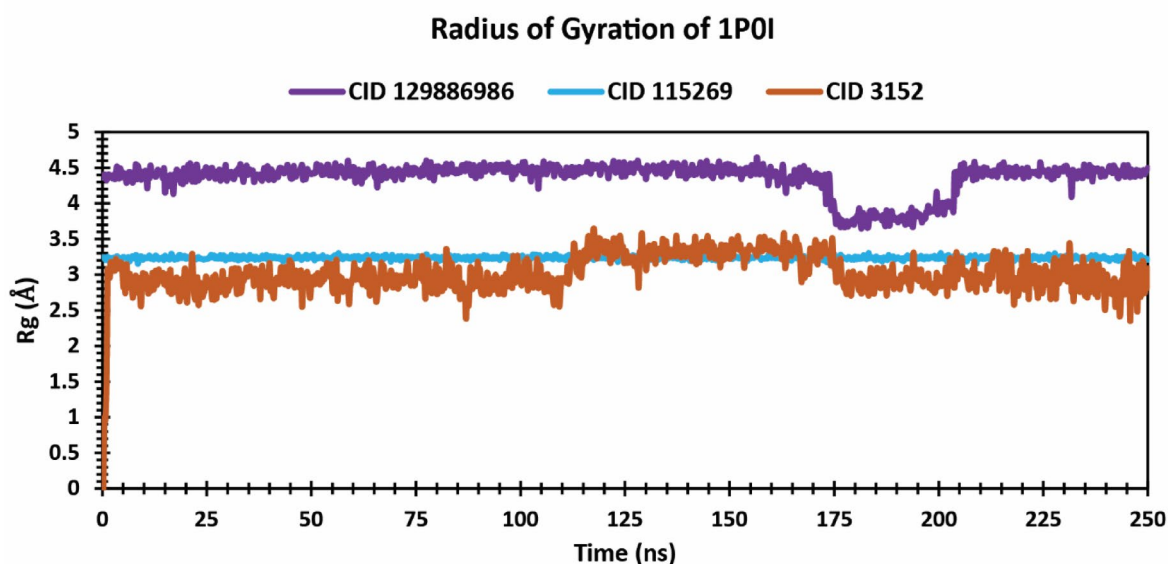


Fig. 7. Rg values of the protein–ligand complexes across a 250 ns simulation timeline. The colors orange, blue, and purple, respectively, represent the complexes of the three compounds CID 3152, CID 115269, and CID 129886986 with 1P0I.

as shown in Fig. 7. Whereas, the compounds CID 129886986 and CID 115269, in complex with 1P0I protein exhibited average Rg values of 4.37 Å and 3.24 Å, respectively which is nearer to the standard compound CID 3152. In comparison to standard CID 3152, CID 115269 in the protein–ligand complex showed a slightly higher Rg value without any distinguishable fluctuations, which indicates its tight binding with the protein. During the whole simulation time, CID 129886986 in the complex with 1P0I protein showed a higher but consistent Rg value. It showed a decrease in Rg value during the 175 to 205 ns timeframe, suggesting conformational change, achieving more compatibility with the protein than at any other moment of the simulation timeframe.

SASA analysis

Solvent Accessible Surface Area (SASA) data were analyzed to assess ligand packing in the protein's active site. Low SASA values indicate tightly packed residues with reduced solvent exposure, while high SASA values suggest greater exposure and looser packing⁶¹. During 250 ns of simulation time, the highest and lowest average SASA values were 102.89 Å² and 85.91 Å² for CID 3152 and CID 129886986 when in complex with 1P0I protein, respectively (Fig. 8). Whereas, CID 115269 in complex with 1P0I protein showed the most consistent SASA value during the entire simulation having an average value of 95.49 Å². Both of our selected compounds showed tight packing with the protein compared to the standard compound. For CID 3152 in the protein–ligand complex, the SASA value exhibited an overall increasing trend throughout the simulation. Initially, it showed a sharp rise to nearly 150 Å² within the first 5 ns, followed by a decline until 13 ns, stabilizing within the 50–100 Å² range. However, significant fluctuations of approximately 180 Å² were observed around 125 ns and 170 ns. In the final 65 ns, the SASA value continued to increase, indicating the progressively looser binding of CID 3152 with the 1P0I protein over time. In complex with the protein, CID 129886986 exhibited a higher SASA value than the standard CID 3152 during the first 65 ns. The value then declined and stabilized within the 50–100 Å² range. After 175 ns, fluctuations were observed, with a brief increase in SASA, indicating greater solvent exposure. However, it later stabilized within the 65–105 Å² range for the remainder of the simulation. In the protein–ligand complex, CID 115269 exhibited a lower SASA value than CID 3152 throughout most of the simulation, with only minor fluctuations, indicating tight and stable packing with the protein and reduced solvent exposure. Fluctuations were observed around 9 ns and 205 ns, but there were no significant fluctuations, further supporting its tight binding with the protein. The SASA data analysis supports the Rg data, both of which demonstrate the compound's superior binding ability.

Principal component analysis

Principal component analysis (PCA) is a computational method to identify and understand the significant coordinated motions among the protein domains during MD simulation⁶². PCA utilizes statistical methods for extracting information on the collective movement of a complex and the stability of the complex in biological systems. The essential variations of the complexes are sorted as principal components and plotted as eigenvectors in response to their variance to form a PCA scatter for analytical purposes⁶³. To achieve a deep knowledge of protein domain motion patterns along with the extent of conformational changes upon ligand binding, PCA analysis was done for the CID 3152-1P0I complex, the CID 115269-1P0I complex, the CID 129886986-1P0I complex, and the apo 1P0I protein. In our study, the chromatic graphs generated from various protein configurations are plotted as dots, each of which indicates a unique configuration. During the simulation, the color of the dots shifts in a time-dependent manner from blue to white to red, indicating the conformational changes within the protein. In Fig. 9, blue portrays the first timestep, while white and red represent the middle and last timesteps, respectively.

PCA revealed three principal components (PCs) through molecular dynamics trajectories, elucidating the motion of a notable segment of the protein structure. From Fig. 9, the apo-protein (1P0I), CID 3152, CID 115269, and CID 129886986 in the system contributed to 21.7%, 22.7%, 29.8%, and 23.1% of the variations, respectively. A higher contribution in variations indicates a destabilization trend, and a lower contribution indicates a stable complex and collective movement in a biological system⁶³. The PC1 value of the standard CID 3152-1P0I complex was 22.7%, and the lowest, except for the PC1 value of apo 1P0I. This suggests fewer conformational changes and higher stability of the complex. Between the CID 115269-1P0I complex and the CID

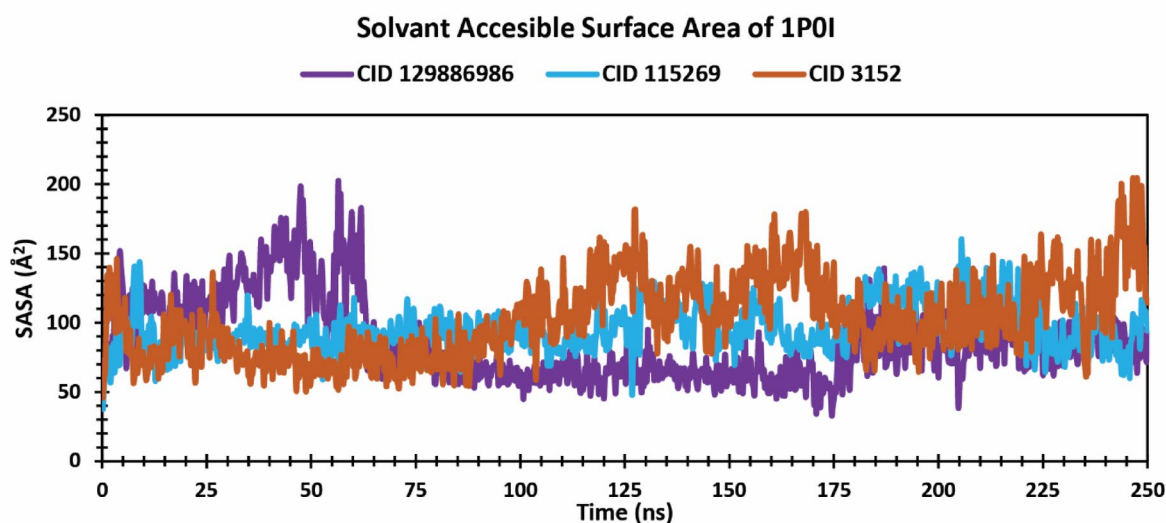


Fig. 8. SASA values of the ligand–protein complexes over the course of the 250 ns simulation. The colors for the protein complexed with CID 3152, CID 115269, and CID 129886986 were orange, blue, and purple, according to this order.

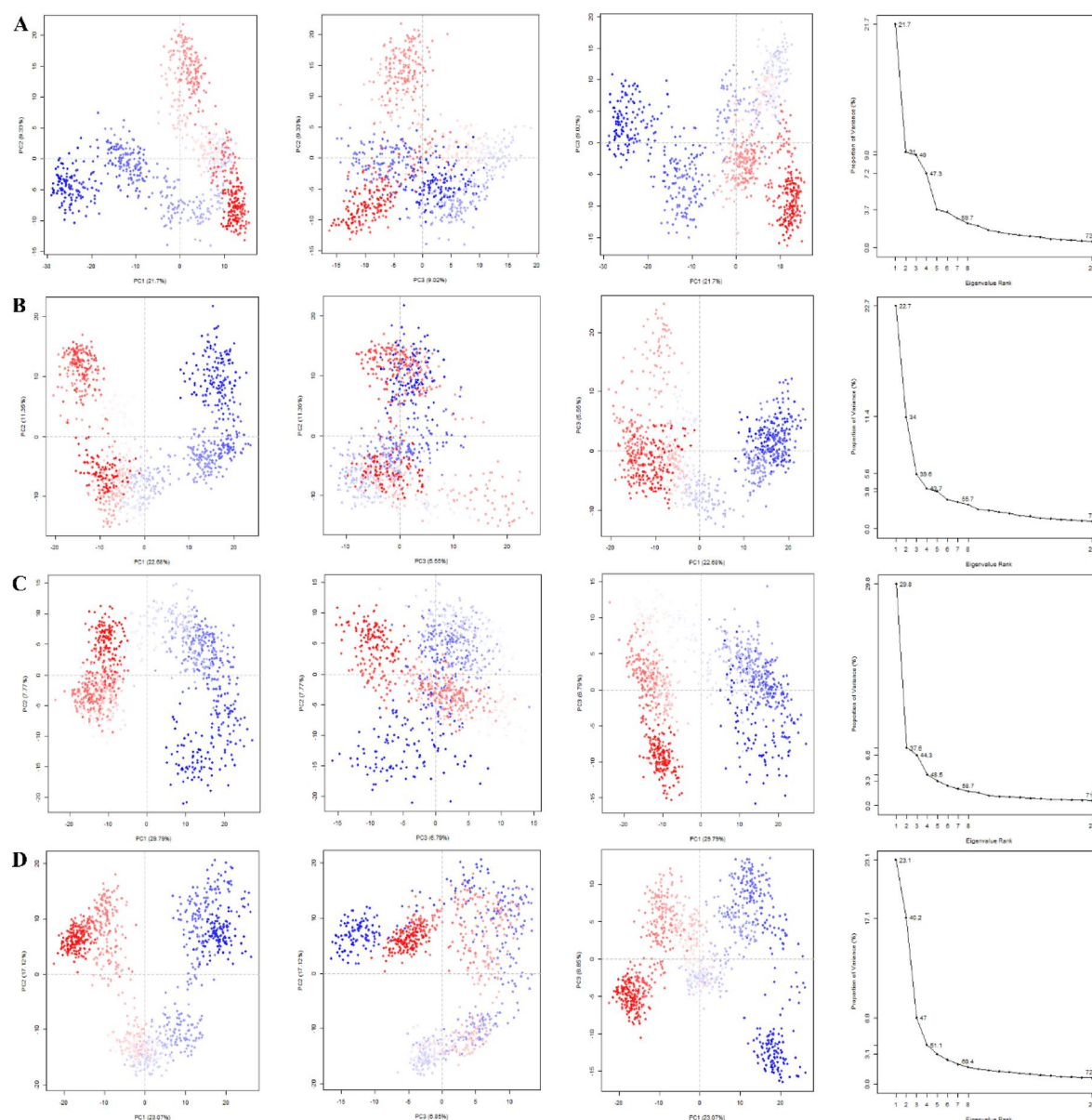


Fig. 9. Graphical representation of the PCA analysis of (A) apo (1P0I) protein, (B) CID 3152-1P0I complex, (C) CID 115269-1P0I complex, (D) CID 129886986-1P0I complex, where red and blue dots show the simulation's illustration of protein conformational changes.

129886986-1P0I complex, the PC1 value for the CID 129886986-1P0I complex was lower and almost exhibited the same stability as the standard ligand–protein complex during the simulation period. It also indicates that the CID 115269-1P0I complex has undergone a larger conformational change than the other mentioned complexes.

Dynamic cross-correlation matrix

The dynamic cross-correlation matrix (DCCM) was applied to investigate the comparative conformational motions of protein–ligand complexes in several simulation systems⁵⁰. To thoroughly understand the conformational changes of the CID 3152-1P0I complex, CID 115269-1P0I complex, CID 129886986-1P0I complex, and apo-protein (1P0I) protein, they were analyzed during a DCCM study under a 250 ns simulation timeframe. Time-dependent correlation coefficient studies among the residues of protein, ranging from -1 to $+1$, are portrayed via two different colors, blue and purple, in Fig. 10, for analyzing the nature of correlation. Various shades of colors portray the correlation level, and darker shades indicate a stronger correlation, either positive or negative. Correlation coefficient values ranging from 0.5 to 1 suggest a strong positive correlation, whereas from -0.5 to -1 suggest a strong negative correlation. A positive correlation indicates the same directional movement of the residues, and a negative correlation indicates the opposite directional movement⁶⁴. In Fig. 10, shades of blue indicate a positive correlation, and shades of purple indicate a negative correlation. Upon analyzing the DCCM diagrams of the four systems, quite significant changes were noticed upon ligand binding. In contrast

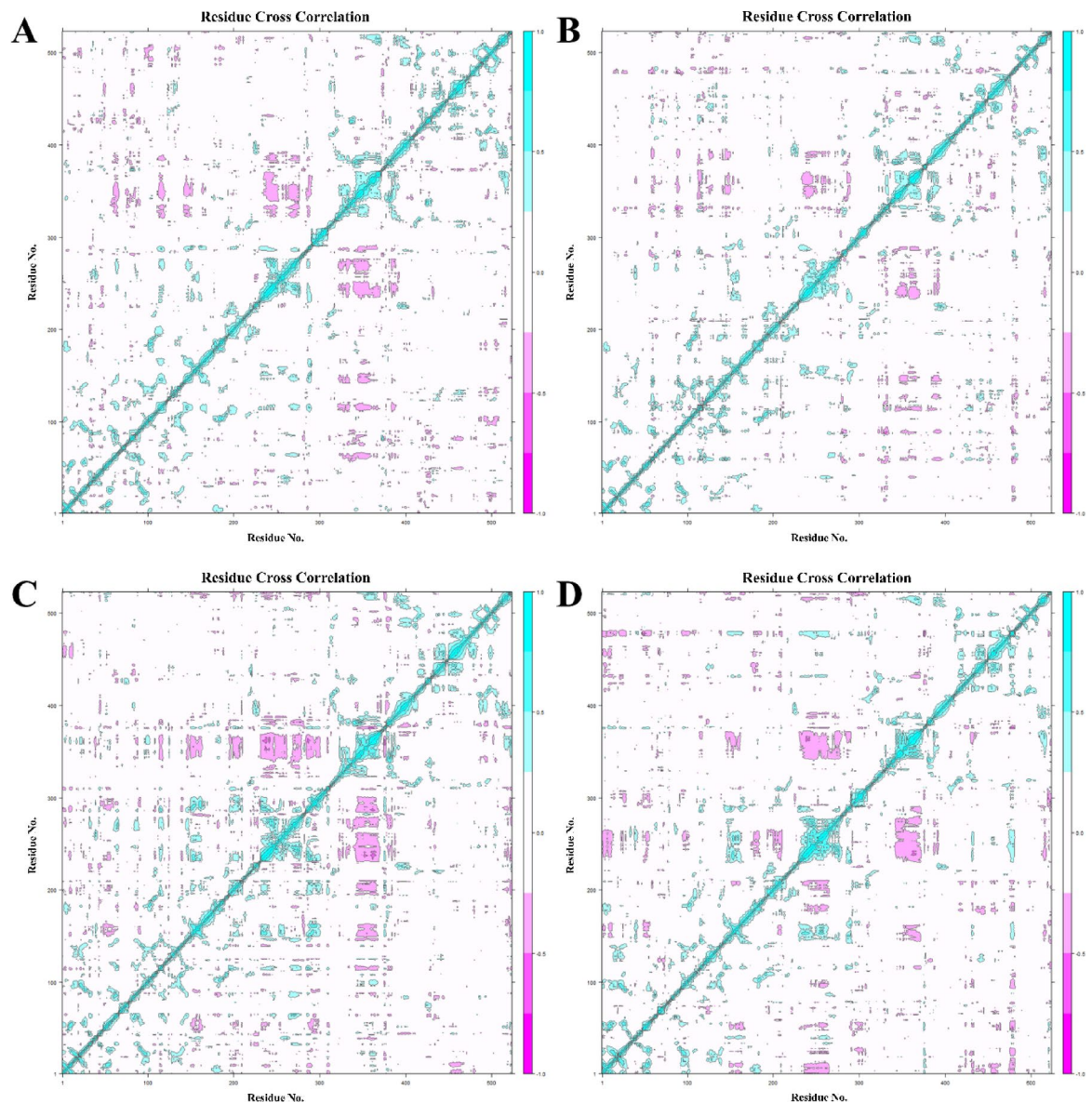


Fig. 10. Ca-residue cross-correlation profiles for (A) apo (1P0I) protein, (B) CID 3152-1P0I complex, (C) CID 115269-1P0I complex, (D) CID 129886986-1P0I complex.

to apo (1P0I), all three other systems showed stable positive correlations, indicating collective movement in the entire complexes along with negative correlations mostly in the range of 300–400 residues. Standard CID 3152-1P0I complex showed fewer negative correlations than any other complexes, indicating its better collective movement upon ligand binding. CID 115269-1P0I complex showed the most opposite directional movement. CID 129886986-1P0I complex showed fewer opposite directional movements than CID 115269-1P0I complex, but higher than CID 3152-1P0I complex and apo 1P0I protein in the mentioned range. The DCCM diagram analysis suggests that the CID 3152-1P0I complex is the most stable, and the CID 129886986-1P0I complex has better stability than the CID 115269-1P0I complex. Within the complex, correlated motions are most readily apparent in the areas highlighted by the dashed black outline.

Free energy landscape analysis

The free energy landscape (FEL) was conducted to observe a clearer perspective on the conformational change of a comprehensive system⁶⁵. In this study, FEL was determined for apo-1P0I, CID3152-1P0I complex, CID115269-1P0I complex, and CID129886986-1P0I complex to understand the lowest free energy of the Ca backbone atoms of proteins in terms of stability. The first two principal components, PC1 and PC2, of the complexes were plotted to form an FEL graph. In Fig. 11, the color change from red to violet denotes a change in Gibbs free energy. Red indicates a high-energy, unstable system, whereas violet indicates a low-energy, more stable system. During stabilization, a complex loses energy, and its energy state changes color from red to violet. Also, a single energy basin confining stable free energy minima indicates a stable structure, but multiple energy basins

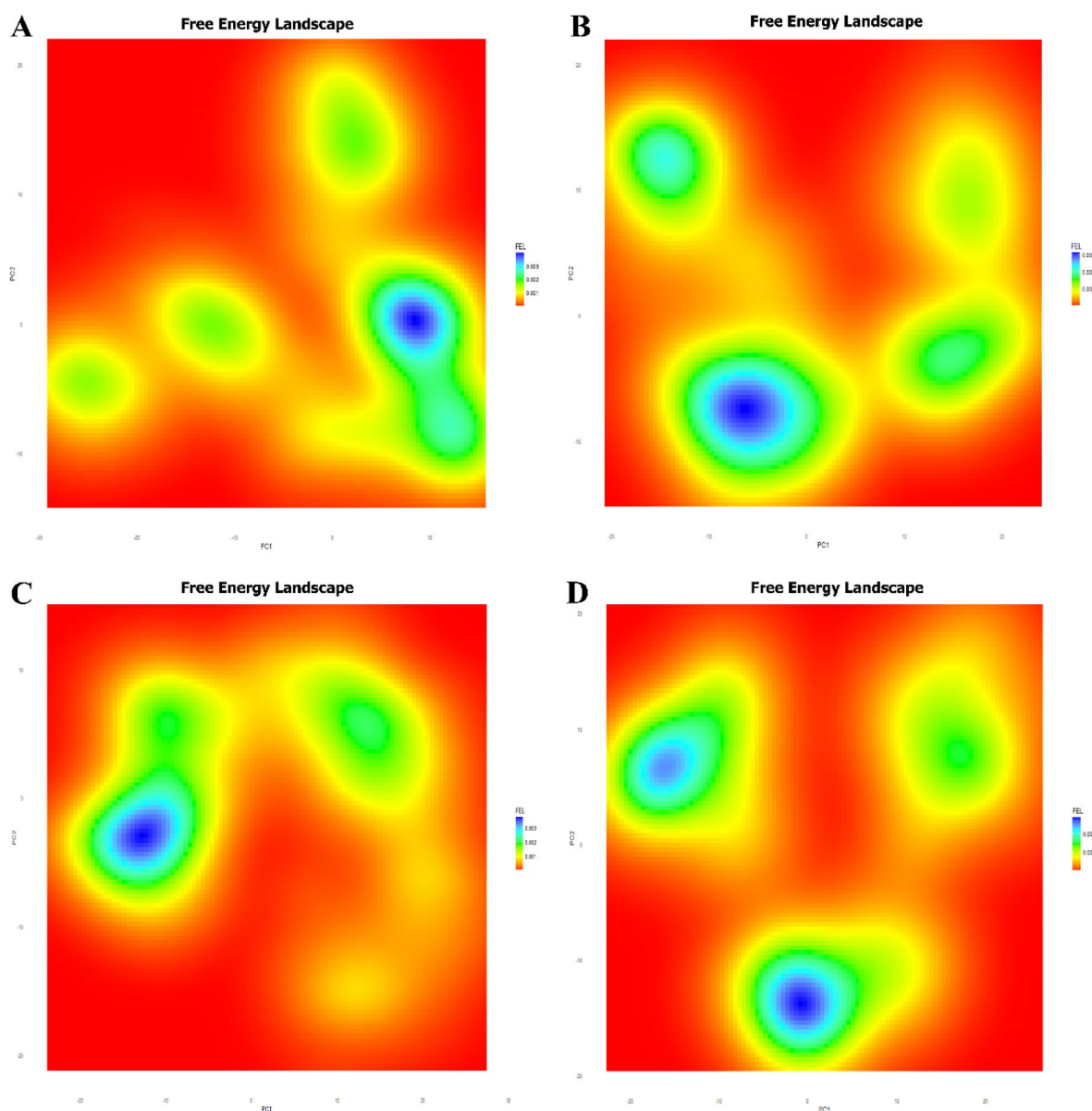


Fig. 11. Free energy landscape (FEL) Analysis for (A) apo (1P0I) protein, (B) CID 3152-1P0I complex, (C) CID 115269-1P0I complex, (D) CID 129886986-1P0I complex. The energy increases in the order of violet < blue < green < yellow < red < dark red.

suggest more conformational change and formation of the loop-like structure⁶⁶. We observed stable free energy minima confined in a single energy basin for the apo (1P0I) protein. All three other complexes showed multiple metastable and expansive energy basins, suggesting their conformational changes over time compared to the apo protein. All the complexes gradually gained stability during the 250 ns simulation period.

Density functional theory

Frontier molecular orbital study

The pharmacological activities of a compound depend on the electronic structure of the compound. The density functional theory (DFT) study was conducted on CID 115269, CID 129886986, and standard ligand CID 3152 to better understand ligand–protein packing by learning their electronic structure. The distribution pattern and energy level of a compound's orbitals determine a compound's reactivity in a system by describing a compound's electronic structure^{47,48}. Energy distribution patterns of the highest occupied molecular orbital (HOMO) and the lowest unoccupied molecular orbital (LUMO), known as the frontier molecular orbital, were studied and analyzed for a better perception of the reactivity of the compounds of our interest. A stable chemical compound shows a minimal energy gap between its HOMO and LUMO levels, suggesting its high reactivity, but an unstable compound exhibits a higher energy gap and lower reactivity as an electronic transition becomes slower between

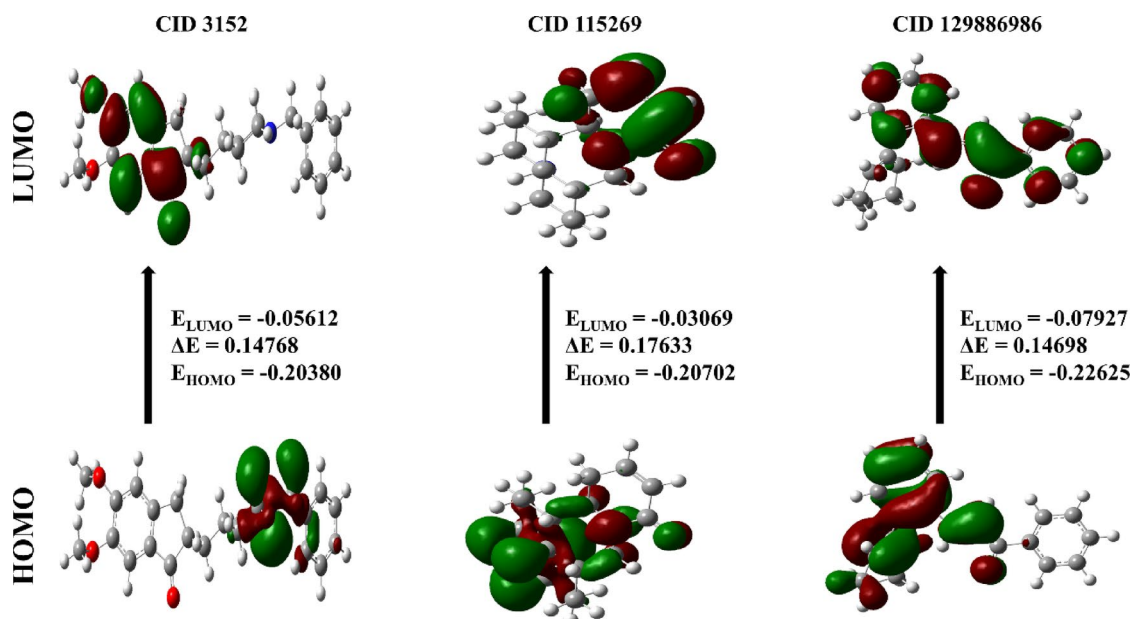


Fig. 12. The HOMO and LUMO molecular orbitals of the selected candidate drug molecules CID 115269, CID 129886986, and standard drug molecule CID 3152.

Features	Ligands		
	CID 3152	CID 115269	CID 129886986
Electronic energy (Eh) (Hartree)	−1212.09409	−769.360696	−887.278202
HOMO energy (au)	−0.2038	−0.20702	−0.22625
LUMO energy (au)	−0.05612	−0.03069	−0.07927
Ionization potential (I)	0.2038	0.20702	0.22625
Electron affinity (A)	0.05612	0.03069	0.07927
Energy gap (EL-EH) (au)	0.14768	0.17633	0.14698
Global hardness (η) (au)	0.07384	0.088165	0.07349
Global Softness (S) (au) ^{−1}	6.771397616	5.67118471	6.803646755
electronegativity (χ) (au)	0.12996	0.118855	0.15276
Chemical potential (μ) (au)	−0.12996	−0.118855	−0.15276
Electrophilicity index(ω) (au)	0.114366208	0.080114053	0.158767299

Table 4. Calculated FMO energies and their corresponding physicochemical descriptors (global hardness, electronegativity, global softness, chemical potential, and electrophilicity index).

lower and higher energy states with the increase of energy gap^{67,68}. Figure 12 shows the HOMO–LUMO orbitals for the compounds.

Table 4 depicted that the HOMO energy levels for the compounds ranged from −0.2038 to −0.22625 eV and the LUMO energy levels ranged from −0.03069 to −0.07927 eV. The energy gaps between the HOMO and LUMO levels of CID 115269, CID 129886986, and CID 3152 were 0.17633 eV, 0.14698 eV, and 0.1476 eV, respectively. CID 129886986 demonstrated the lowest energy gap among the compounds, suggesting higher reactivity than CID 115269 and CID 3152.

Quantum quality descriptors

Chemical descriptors portray a valid scene of the chemical behaviors of a chemical compound or physiologically active molecule. The nature of a compound in a biological system is influenced by its chemical characteristics. A DFT study was done following Koopmans' theorem, which gives an idea of the electric characteristics of a compound by analyzing its chemical characteristics, including electronic energy, HOMO–LUMO energy, ionization potential, electron affinity, global hardness, global softness, electronegativity, chemical potentials, and electrophilicity index⁶⁹. These quantitative values are presented in Table 4.

A compound's reactivity depends on its ability to give and receive electrons. CID 3152, CID 115269, and CID 129886986 showed electron affinity values of 0.05612, 0.03069, and 0.07927, along with electronegativity values of 0.12996, 0.118855, and 0.15276, respectively. Though all three compounds showed signs of strong

binding affinity and stability, CID 129886986, having the highest electron affinity value and electronegativity value, suggests that it can bind strongly and form a more stable complex than the other two compounds⁷⁰. Also, other chemical behaviors shown in the table indicate the same. All three compounds reflected a strong electrophilic nature, suggesting high reactivity with tight binding, and demonstrated almost the same behavior in all categories⁷¹.

Discussion

BuChE is a key target for Alzheimer's disease (AD) drug development, as its increased activity in the brain is associated with A β plaque formation, cerebral amyloid angiopathy, and neurofibrillary tangles (NFTs)⁷². Elevated BuChE expression significantly correlates with cognitive decline in AD patients, while in transgenic mouse models, it accelerates plaque maturation⁷³. Additionally, BuChE mutations, particularly the variant K, worsen AD progression through synergy with the $\epsilon 4$ allele of Apolipoprotein E⁷⁴. Inhibiting BuChE activity may help reduce disease severity and serve as a promising therapeutic approach for AD. Natural dietary compounds serve as potential bioactive agents in mitigating various cancers, diabetes, pain, and neurological illnesses, including Parkinson's and Huntington's diseases^{75–77}. In our study, we isolated 44 dietary compounds from different medicinal plants through literature reviews to screen the potential inhibitors against BuChE to combat AD.

Computer-aided drug design (CADD) is a combination of several advanced computational approaches used as a tool in the determination and development of promising drug candidates for a target protein⁷⁸. A variety of methods, including molecular docking, MM-GBSA, ADMET, and MD simulation, were employed in the identification and development of potent drug candidates^{78,79}. Molecular docking facilitates the identification of potent drug candidates by screening large compound libraries. It provides insights into molecular-level interactions by evaluating site-specific binding affinity between target proteins and compounds⁸⁰. We initially screened 44 compounds, identifying three (CID 445154, CID 115269, and CID 129886986) that exhibited strong binding affinity with the 1P0I protein during molecular docking, as shown in Table 1, and Fig. 2. The identified three compounds CID 445154, CID 115269 and CID 129886986 formed significant numbers of hydrogen bonds, hydrophobic bonds, and other bonds with the BuChE protein (Table 2).

According to the ΔG -Bind score determined by the MM-GBSA, a lower value indicates a better docking result⁸¹. For CID 115269 and CID 129886986, the ΔG -Bind scores were lower than the other docked compounds, appearing to be the best resulting docked compounds (Fig. 3). To evaluate whether a molecule qualifies as a drug candidate, ADME and toxicity analysis provide information on the compound's pharmacokinetic characteristics and toxicity effects in biological systems and nature⁸². During ADME and toxicity analysis, both CID 115269 and CID 129886986 exhibited quite promising results. In terms of Lipinski's rule of five, with a slightly higher Log Po/w(MLOGP) value than drug-like molecules, CID 129886986 violated only one rule, whereas CID 115269 didn't violate any. Both compounds even showed a less toxic effect in comparison to standard CID 3152 (Table 3).

In this study, a 250 ns MD simulation was performed to observe the structural stability of the ligand-macromolecule complex within the biological system. Parameters, including RMSD, RMSF, Rg, and SASA values, were analyzed to get a clearer picture of the stability of the complexes. To understand the integrity of the conformation of the complexes, we thoroughly examined the RMSD value, where the lower values suggest better conformational stability. A stable system exhibits a plateau in RMSD, while continuous increases may indicate unfolding or instability^{59,83}. Functionally dynamic protein regions were assessed from the analysis of the RMSF values obtained. Active sites or loops within the protein tend to exhibit a higher RMSF value, while a low value demonstrates the rigid nature of the structure. Over a 250-simulation period, the two identified compounds, CID 115269 and CID 129886986, showcased lower RMSD values when complexed with the receptor, representing the structural stability of the complexes, presented in Fig. 4, and Fig. 5. RMSF values give a perspective on the conformational stability and structural flexibility of Ca atoms⁸⁴. The RMSF values obtained from the 1P0I-CID 115269 and 1P0I-CID 129886986 complexes suggested high stability, maintaining their structural integrity within the complexes with a few fluctuations compared to the standard drug (Fig. 6). The compactness of the complexes was evaluated using Rg values, which reflect the relationship between structural stability and compactness. Fluctuations in Rg trajectories during the simulation indicate either protein folding into a more stable state or unfolding due to conformational expansion. A decreasing Rg trend suggests protein folding into a stable form, while an increasing trend indicates unfolding or denaturation⁶⁰. According to the Rg values described in (Fig. 7), the protein complexed with CID 115269 exhibited better compactness in comparison to the CID 129886986-protein complex. Another parameter to observe the stability of the complexes by packing ligands in the active sites of the protein is extracting the SASA values of protein-ligand complexes. The lower values of SASA indicate tight packing of the ligand within the complex and less exposure to the solvent⁶¹. In our findings, the 1P0I-CID 129886986 complex showed a lower average SASA value than the 1P0I-CID 115269 complex (Fig. 8). Interestingly, both complexes showed lower SASA values in comparison to the standard CID 3152-protein complex.

On ligand-protein complexes, the PCA, FEL, and DCCM analyses were performed. PCA analysis was employed to identify key coordinated motions within protein domains during the simulation⁶². PCA identifies dominant conformational changes in proteins by processing large datasets to extract meaningful biological insights. It reduces dimensionality by representing atomic coordinates from MD trajectories as principal components (PCs), enabling the visualization and interpretation of global motions instead of analyzing individual atomic fluctuations. Based on PCA analysis results, the performance of the 1P0I-CID 129886986 combination was almost identical to that of the standard drug-protein complex, suggesting nearly equal stability for both. These findings suggest that compared to the two complexes, the 1P0I-CID 115269 complex may have a comparatively larger conformational shift (Fig. 9). To comprehend the conformational change of complexes

within a complete system, FEL analysis was performed. FEL reveals information about the low-energy and high-energy states of the complexes by mapping out the conformational landscape⁶⁶. In comparison to the apoprotein, the 1P01-CID 115269 and 1P01-CID 129886986 complexes both showed conformational changes throughout the 250 ns simulation; however, as the simulation went on, they eventually became stable (Fig. 10). The relative conformational movements of complexes within various simulation systems were identified using DCCM⁶⁴. DCCM analysis was used to determine the correlated motion of protein domains during MD simulation. It captures the collective behavior of atoms, residues, or domains to identify coupled movements influencing protein function, stability, and ligand interactions. The cross-correlation coefficient of atomic fluctuations reveals how the motion of one residue affects another. In our DCCM studies, the CID 129886986-protein complex topped the CID 115269-protein complex in terms of stability (Fig. 11). To better examine the reactivity of CID 115269 and CID 129886986, a DFT investigation was carried out. CID 129886986 showed higher reactivity with a smaller energy difference between the HOMO and LOMO levels, however, CID 115269 showed about the same amount of reactivity in comparison to regular CID 3152 (Fig. 12). To estimate the compounds' binding affinities and stability, a number of their chemical properties was examined. CID 129886986 was identified as the strongest binder, forming the most stable complex. Both compounds exhibited significant electrophilicity, highlighting their strong binding affinity and stable complex-forming capabilities⁷⁰.

The results indicate that CID 115269 and CID 129886986 are promising candidates for inhibiting the BuChE protein. Although several clinical trial methods are required to qualify as a successfully approved drug, these two compounds may have the ability to improve AD conditions.

Conclusion

Butyrylcholinesterase (BuChE) plays a significant role in Alzheimer's disease (AD) by contributing to cholinergic dysfunction and influencing the accumulation of amyloid plaques, a hallmark of AD. Currently, there is no viable treatment to cure AD. In our study, we screened butyrylcholinesterase (BuChE) inhibitors from a library of 44 compounds derived from dietary plants, based on a comprehensive literature review. Among them, two compounds, CID 115269 and CID 129886986, were identified through molecular docking and MM/GBSA analyses, followed by ADME and toxicity assessments that confirmed their pharmacokinetics and safety profiles. MD simulations, along with post-simulation analyses including PCA, DCCM, and FEL analysis, confirmed the structural stability of these compounds at BuChE's active site, highlighting their potential as effective inhibitors. Additionally, DFT calculation analysis of the identified compounds showed improved reactivity and binding affinity, highlighting them as promising drug candidates for AD. Nevertheless, further in vitro and in vivo studies are required to confirm their efficacy against BuChE.

Data availability

The datasets generated and/or analyzed during the current study are available in the RCSB Protein Data Bank repository at <https://www.rcsb.org/>. Besides, additional data is provided within the manuscript and supplementary information files.

Received: 1 February 2025; Accepted: 9 April 2025

Published online: 17 May 2025

References

1. Masters, C. L. et al. Alzheimer's disease. *Nat. Rev. Dis. Primers* **1**, 1–18 (2015).
2. Li, X. et al. Global, regional, and national burden of Alzheimer's disease and other dementias, 1990–2019. *Front Aging Neurosci* **14** (2022).
3. Roy, N., Hassan, A.-M., Alom, R., Rajib, Md. H. R. & Al-Mamun, K. A. The situation of Alzheimer's disease in Bangladesh: Facilities, expertise, and awareness among general people. *J. Neurol. Disord.* **8**, 1–7 (2020).
4. Livingston, G. et al. Dementia prevention, intervention, and care: 2020 report of the Lancet commission. *Lancet* **396**, 413–446 (2020).
5. Jasiński, J., Targońska, M. & Wasąg, B. The role of butyrylcholinesterase and iron in the regulation of cholinergic network and cognitive dysfunction in Alzheimer's disease pathogenesis. *Int. J. Mol. Sci.* **22**, 1–14 (2021).
6. Hampel, H. et al. The amyloid- β pathway in Alzheimer's disease. *Mol. Psychiatry* **26**, 5481–5503 (2021).
7. Kamatham, P. T., Shukla, R., Khatri, D. K. & Vora, L. K. Pathogenesis, diagnostics, and therapeutics for Alzheimer's disease: Breaking the memory barrier. *Ageing Res. Rev.* <https://doi.org/10.1016/j.arr.2024.102481> (2024).
8. Zhang, H. et al. Interaction between A β and Tau in the pathogenesis of Alzheimer's disease. *Int. J. Biol. Sci.* **17**, 2181–2192 (2021).
9. Wang, L. et al. Tau degradation in Alzheimer's disease: Mechanisms and therapeutic opportunities. *Alzheimer's Dementia* **21**, e70048 (2025).
10. Pathak, C. & Kabra, U. D. A comprehensive review of multi-target directed ligands in the treatment of Alzheimer's disease. *Bioorg. Chem.* **144**, 107152 (2024).
11. Lane, R. M., Potkin, S. G. & Enz, A. Targeting acetylcholinesterase and butyrylcholinesterase in dementia. *Int. J. Neuropsychopharmacol.* **9**, 101–124. <https://doi.org/10.1017/S1461145705005833> (2006).
12. Kulaga, D. et al. Discovery of new dual butyrylcholinesterase (BuChE) inhibitors and 5-HT7 receptor antagonists as compounds used to treat Alzheimer's disease symptoms. *Biomed. Pharmacother.* **186**, 117995 (2025).
13. Marucci, G. et al. Efficacy of acetylcholinesterase inhibitors in Alzheimer's disease. *Neuropharmacology* **190**, 108352 (2021).
14. Darvesh, S. et al. Butyrylcholinesterase is associated with β -amyloid plaques in the transgenic APPSWE/PSEN1dE9 mouse model of Alzheimer disease. *J. Neuropathol. Exp. Neurol.* **71**, 2–14 (2012).
15. Wang, Z. et al. Butyrylcholinesterase K variant and Alzheimer's disease risk: A meta-analysis. *Med. Sci. Monit.* **21**, 1408–1413 (2015).
16. Mitra, S. et al. Tacrine derivatives in neurological disorders: focus on molecular mechanisms and neurotherapeutic potential. *Oxid. Med. Cell. Longevity* <https://doi.org/10.1155/2022/7252882> (2022).
17. Businaro, R. et al. Therapeutic opportunities for food supplements in neurodegenerative disease and depression. *Front. Nutr.* **8**, 669846 (2021).

18. Bigford, G. E. & Del Rossi, G. Supplemental substances derived from foods as adjunctive therapeutic agents for treatment of neurodegenerative diseases and disorders. *Adv. Nutr.* **5**, 394–403 (2014).
19. Deshpande, P., Gogia, N. & Singh, A. Exploring the efficacy of natural products in alleviating Alzheimer's disease. *Neural Regen. Res.* **14**, 1321 (2019).
20. Shaker, B., Ahmad, S., Lee, J., Jung, C. & Na, D. In silico methods and tools for drug discovery. *Comput. Biol. Med.* **137**, 104851 (2021).
21. Cuffaro, D., Digiaco, M. & Macchia, M. Dietary bioactive compounds: implications for oxidative stress and inflammation. *Nutrients* **15**, 4966 (2023).
22. Saur, I. M. L., Panstruga, R. & Schulze-Lefert, P. NOD-like receptor-mediated plant immunity: from structure to cell death. *Nat. Rev. Immunol.* **21**, 305–318 (2021).
23. van Zundert, G. C. P., Moriarty, N. W., Sobolev, O. V., Adams, P. D. & Borrelli, K. W. Macromolecular refinement of X-ray and cryoelectron microscopy structures with Phenix/OPLS3e for improved structure and ligand quality. *Structure* **29**, 913–921 (2021).
24. Madhavi Sastry, G., Adzhigirey, M., Day, T., Annabhimoju, R. & Sherman, W. Protein and ligand preparation: Parameters, protocols, and influence on virtual screening enrichments. *J. Comput. Aided Mol. Des.* **27**, 221–234 (2013).
25. Park, H., Zhou, G., Baek, M., Baker, D. & DiMaio, F. Force field optimization guided by small molecule crystal lattice data enables consistent sub-angstrom protein-ligand docking. *J. Chem. Theory Comput.* **17**, 2000–2010 (2021).
26. Siddiquee, N. H. et al. Unveiling the antiviral activity of 2',3,5,7-Tetrahydroxyflavanone as potential inhibitor of chikungunya virus envelope glycoprotein. *Inform. Med. Unlocked* **47**, 101486 (2024).
27. Uddin, M. J. et al. Neuropharmacological assessment and identification of possible lead compound (apomorphine) from *Hygrophila spinosa* through in-vivo and in-silico approaches. *J. Biomol. Struct. Dyn.* <https://doi.org/10.1080/07391102.2024.2317974> (2024).
28. Kim, S. et al. PubChem in 2021: New data content and improved web interfaces. *Nucleic Acids Res.* **49**, D1388–D1395 (2021).
29. Sarkar, K. K. et al. Exploring antioxidative, cytotoxic and neuropharmacological insights into *Bixa orellana* leaves: Experimental and in silico approaches. *Heliyon* **10**, e27001 (2024).
30. Talukder, Md. E. K. et al. Molecular docking, QSAR, and simulation analyses of EGFR-targeting phytochemicals in non-small cell lung cancer. *J. Mol. Struct.* **1321**, 139924 (2025).
31. Islam, Md. T. et al. In silico-based identification of natural inhibitors from traditionally used medicinal plants that can inhibit dengue infection. *Mol. Biotechnol.* <https://doi.org/10.1007/s12033-024-01204-8> (2024).
32. Ngan, C.-H. et al. FTSite: high accuracy detection of ligand binding sites on unbound protein structures. *Bioinformatics* **28**, 286–287 (2012).
33. Islam, M. T. et al. Identification of acetylcholinesterase inhibitors from traditional medicinal plants for Alzheimer's disease using in silico and machine learning approaches. *RSC Adv* **14**, 34620–34636 (2024).
34. Islam, M. T. et al. Uncovering the natural inhibitors from medicinal plants to alleviate human cancers targeting the p53 Protein: An in silico approach. *ChemistrySelect* **10**, e202404160 (2025).
35. Zhou, W., Wang, Y., Lu, A. & Zhang, G. Systems pharmacology in small molecular drug discovery. *Int. J. Mol. Sci.* **17**, 1–16 (2016).
36. Daina, A., Michielin, O. & Zoete, V. SwissADME: A free web tool to evaluate pharmacokinetics, drug-likeness and medicinal chemistry friendliness of small molecules. *Sci. Rep.* **7**, 1–13 (2017).
37. Pires, D. E. V., Kaminskas, L. M. & Ascher, D. B. Prediction and optimization of pharmacokinetic and toxicity properties of the ligand. In *Computational drug discovery and design* 271–284 (2018).
38. Islam, F., Aktaruzzaman, Md., Islam, Md. T., Rodru, F. I. & Yesmine, S. Comprehensive metabolite profiling and evaluation of anti-nociceptive and anti-inflammatory potencies of *Nypa fruticans* (Wurmb.) leaves: Experimental and in-silico approaches. *Heliyon* **11**, e42074 (2025).
39. Saif, A. et al. Pan-cancer analysis of CDC7 in human tumors: Integrative multi-omics insights and discovery of novel marine-based inhibitors through machine learning and computational approaches. *Comput. Biol. Med.* **190**, 110044 (2025).
40. Hosen, M. E. et al. Molecular docking and dynamics simulation approach of *Camellia sinensis* leaf extract derived compounds as potential cholinesterase inhibitors. *Silico Pharmacol.* **11**, 14 (2023).
41. Alsaif, N. A., Wani, T. A., Bakheit, A. H. & Zargar, S. Multi-spectroscopic investigation, molecular docking and molecular dynamic simulation of competitive interactions between flavonoids (quercetin and rutin) and sorafenib for binding to human serum albumin. *Int. J. Biol. Macromol.* **165**, 2451–2461 (2020).
42. Maruyama, Y., Igarashi, R., Ushiku, Y. & Mitsutake, A. Analysis of protein folding simulation with moving root mean square deviation. *J. Chem. Inf. Model* **63**, 1529–1541 (2023).
43. Han, Y., Wang, Z., Ren, J., Wei, Z. & Li, J. Potential inhibitors for the novel coronavirus (SARS-CoV-2). *Brief Bioinform.* **22**, 1225–1231 (2021).
44. Khan, R. J. et al. Targeting SARS-CoV-2: a systematic drug repurposing approach to identify promising inhibitors against 3C-like proteinase and 2'-O-ribose methyltransferase. *J. Biomol. Struct. Dyn.* **39**, 2679–2692 (2021).
45. Wang, Y., Zhou, Y. & Khan, F. I. Molecular insights into structural dynamics and binding interactions of selected inhibitors targeting SARS-CoV-2 main protease. *Int. J. Mol. Sci.* **25**, 13482 (2024).
46. Ali, S., Hassan, Md., Islam, A. & Ahmad, F. A review of methods available to estimate solvent-accessible surface areas of soluble proteins in the folded and unfolded states. *Curr. Protein Pept. Sci.* **15**, 456–476 (2014).
47. Pritchard, B. P., Altarawy, D., Didier, B., Gibson, T. D. & Windus, T. L. New basis set exchange: An open, up-to-date resource for the molecular sciences community. *J. Chem. Inf. Model* **59**, 4814–4820 (2019).
48. Hickey, A. L. & Rowley, C. N. Benchmarking quantum chemical methods for the calculation of molecular dipole moments and polarizabilities. *ACS Publ.* **118**, 3678–3687 (2014).
49. Aktaruzzaman M., Islam M. T., Rakib M. A., Sikdar B., Rehman S., Rahman M. S., Comprehensive Evaluation of the Neuropharmacological Potential of Methanolic Leaf Extract of *Acanthus ebracteatus* (Vahl.) Using Experimental and In Silico Approaches. *Chem. Biodiversity* <https://doi.org/10.1007/s11030-024-10838-4> (2025).
50. Kumari, M., Singh, R. & Subbarao, N. Exploring the interaction mechanism between potential inhibitor and multi-target Mur enzymes of mycobacterium tuberculosis using molecular docking, molecular dynamics simulation, principal component analysis, free energy landscape, dynamic cross-correlation matrices, vector movements, and binding free energy calculation. *J. Biomol. Struct. Dyn.* **40**, 13497–13526 (2022).
51. David, C. C. & Jacobs, D. J. Principal Component Analysis: A Method for Determining the Essential Dynamics of Proteins 193–226. https://doi.org/10.1007/978-1-62703-658-0_11 (2014).
52. Mir, S. A. et al. Exploring KRas protein dynamics: An integrated molecular dynamics analysis of KRas wild and mutant variants. *ACS Omega* **9**, 30665–30674 (2024).
53. Liu, W., Liu, Z., Liu, H., Westerhoff, L. M. & Zheng, Z. Free energy calculations using the movable type method with molecular dynamics driven protein-ligand sampling. *J. Chem. Inf. Model* **62**, 5645–5665 (2022).
54. Kasahara, K., Fukuda, I. & Nakamura, H. A novel approach of dynamic cross correlation analysis on molecular dynamics simulations and its application to Ets1 dimer–DNA complex. *PLoS ONE* **9**, e112419 (2014).
55. Srinivasan, E. & Rajasekaran, R. Effect of β -cyclodextrin-EGCG complexation against aggregated α -synuclein through density functional theory and discrete molecular dynamics. *Chem. Phys. Lett.* **717**, 38–46 (2019).
56. Saikia, S. & Bordoloi, M. Molecular docking: Challenges, advances and its use in drug discovery perspective. *Curr. Drug Targets* **20**, 501–521 (2019).
57. Roskoski, R. Properties of FDA-approved small molecule protein kinase inhibitors. *Pharmacol. Res.* **144**, 19–50 (2019).

58. Hollingsworth, S. A. & Dror, R. O. Molecular dynamics simulation for all. *Neuron* **99**, 1129–1143 (2018).
59. Adelusi, T. I. et al. Molecular modeling in drug discovery. *Inform. Med. Unlocked* **29**, 100880 (2022).
60. Mahmud, S. et al. Virtual screening and molecular dynamics simulation study of plant-derived compounds to identify potential inhibitors of main protease from SARS-CoV-2. *Brief Bioinform.* **22**, 1402–1414 (2021).
61. Qin, X., Zhong, J. & Wang, Y. A mutant T1 lipase homology modeling, and its molecular docking and molecular dynamics simulation with fatty acids. *J. Biotechnol.* **337**, 24–34 (2021).
62. Ghorbani, M., Brooks, B. R. & Klauda, J. B. Critical sequence hotspots for binding of novel coronavirus to angiotensin converter enzyme as evaluated by molecular simulations. *J. Phys. Chem. B* **124**, 10034–10047 (2020).
63. Ali, M. A. et al. Exploring the therapeutic potential of *Petiveria alliacea* L. phytochemicals: A computational study on inhibiting SARS-CoV-2's main protease (Mpro). *Molecules* **29**, 2524 (2024).
64. Akash, S. et al. Novel computational and drug design strategies for inhibition of human papillomavirus-associated cervical cancer and DNA polymerase theta receptor by Apigenin derivatives. *Sci. Rep.* **13**, 16565 (2023).
65. Ahmad, N. et al. Molecular dynamics simulation of zika virus NS5 RNA dependent RNA polymerase with selected novel non-nucleoside inhibitors. *J. Mol. Struct.* **1203**, 127428 (2020).
66. Ahamad, S., Hema, K., Ahmad, S., Kumar, V. & Gupta, D. Insights into the structure and dynamics of SARS-CoV-2 spike glycoprotein double mutant L452R–E484Q. *3 Biotech* **12**, 87 (2022).
67. Panwar, U. & Singh, S. K. Atom-based 3D-QSAR, molecular docking, DFT, and simulation studies of acylhydrazones, hydrazine, and diazene derivatives as IN-LEDGF/p75 inhibitors. *Struct. Chem.* **32**, 337–352 (2021).
68. Arivazhagan, R., Sridevi, C. & Prakasam, A. Exploring molecular structure, spectral features, electronic properties and molecular docking of a novel biologically active heterocyclic compound 4-phenylthiosemicarbazide. *J. Mol. Struct.* **1232**, 129956 (2021).
69. Tsuneda, T., Song, J.-W., Suzuki, S. & Hirao, K. On Koopmans' theorem in density functional theory. *J. Chem. Phys.* **133** (2010).
70. Karton, A. & Spackman, P. R. Evaluation of density functional theory for a large and diverse set of organic and inorganic equilibrium structures. *J. Comput. Chem.* **42**, 1590–1601 (2021).
71. Srivastava, R. Theoretical studies on the molecular properties, toxicity, and biological efficacy of 21 new chemical entities. *ACS Omega* **6**, 24891–24901 (2021).
72. Macdonald, I. R. et al. Quantification of butyrylcholinesterase activity as a sensitive and specific biomarker of Alzheimer's disease. *J. Alzheimer's Dis.* **58**, 491–505 (2017).
73. Reale, M. et al. Expression profiling of cytokine, cholinergic markers, and amyloid- β deposition in the APPSWE/PS1dE9 mouse model of Alzheimer's disease pathology. *J. Alzheimer's Dis.* **62**, 467–476 (2018).
74. Ratis, R. C. et al. Confirmed synergy between the $\epsilon 4$ allele of apolipoprotein E and the variant K of butyrylcholinesterase as a risk factor for Alzheimer's disease: A systematic review and meta-analysis. *J. Alzheimer's Dis. Rep.* **7**, 613–625 (2023).
75. Wu, J.-C. et al. Chemopreventive effect of natural dietary compounds on xenobiotic-induced toxicity. *J. Food Drug Anal.* **25**, 176–186 (2017).
76. Uddin, M. J. et al. Isolation and quantification of caffeine in marketed tea and carbonated beverage products in Bangladesh. *Toxicol. Anal. Clin.* <https://doi.org/10.1016/j.toxac.2024.09.001> (2024).
77. Hasan, A. R. et al. The alteration of microglial calcium homeostasis in central nervous system disorders: A comprehensive review. *Neuroglia* **5**, 410–444 (2024).
78. Bharatam, P. V. Computer-Aided Drug Design. In *Drug Discovery and Development* 137–210 (Springer Singapore, Singapore, 2021). https://doi.org/10.1007/978-981-15-5534-3_6.
79. Yu, W. & MacKerell, A. D. Computer-Aided Drug Design Methods 85–106. https://doi.org/10.1007/978-1-4939-6634-9_5 (2017).
80. Sabe, V. T. et al. Current trends in computer aided drug design and a highlight of drugs discovered via computational techniques: A review. *Eur. J. Med. Chem.* **224**, 113705 (2021).
81. Elfiky, A. A., Mahran, H. A., Ibrahim, I. M., Ibrahim, M. N. & Elshemey, W. M. Molecular dynamics simulations and MM-GBSA reveal novel guanosine derivatives against SARS-CoV-2 RNA dependent RNA polymerase. *RSC Adv.* **12**, 2741–2750 (2022).
82. Kar, S. & Leszczynski, J. Open access in silico tools to predict the ADMET profiling of drug candidates. *Expert Opin. Drug Discov.* **15**, 1473–1487 (2020).
83. Wu, N. et al. Elucidation of protein–ligand interactions by multiple trajectory analysis methods. *Phys. Chem. Chem. Phys.* **26**, 6903–6915 (2024).
84. Rai, H. et al. Molecular docking, binding mode analysis, molecular dynamics, and prediction of ADMET/toxicity properties of selective potential antiviral agents against SARS-CoV-2 main protease: An effort toward drug repurposing to combat COVID-19. *Mol. Divers.* **25**, 1905–1927 (2021).

Acknowledgements

This study was supported by Princess Nourah bint Abdulrahman University Researchers Supporting Project number (PNURSP2025R30), Princess Nourah bint Abdulrahman University, Riyadh, Saudi Arabia. This research was funded by the Researchers Supporting Project number (RSPD2025R811), King Saud University, Riyadh, Saudi Arabia.

Author contributions

M.T.I. and M.A. performed Conceptualization; M.T.I., M.A., C.B., F.I.R., P.S., A.R.H., T.T., and H.A.D. analyzed the Data; M.T.I., M.A., C.B., F.I.R., and P.S. wrote the Manuscript; G.M.A., M.Q.A.G., A.A.S., M.M.A.D., K.K.S., and M.O.R. supervised and reviewed the manuscript. All authors read and approved the final manuscript.

Funding

This study was supported by Princess Nourah bint Abdulrahman University Researchers Supporting Project number (PNURSP2025R30), Princess Nourah bint Abdulrahman University, Riyadh, Saudi Arabia. This research was funded by the Researchers Supporting Project number (RSPD2025R811), King Saud University, Riyadh, Saudi Arabia.

Declarations

Competing interests

The authors declare no competing interests.

Additional information

Supplementary Information The online version contains supplementary material available at <https://doi.org/10.1038/s41598-025-98092-y>

[0.1038/s41598-025-98092-y](https://doi.org/10.1038/s41598-025-98092-y).

Correspondence and requests for materials should be addressed to M.T.I., M.A., K.K.S. or M.O.R.

Reprints and permissions information is available at www.nature.com/reprints.

Publisher's note Springer Nature remains neutral with regard to jurisdictional claims in published maps and institutional affiliations.

Open Access This article is licensed under a Creative Commons Attribution-NonCommercial-NoDerivatives 4.0 International License, which permits any non-commercial use, sharing, distribution and reproduction in any medium or format, as long as you give appropriate credit to the original author(s) and the source, provide a link to the Creative Commons licence, and indicate if you modified the licensed material. You do not have permission under this licence to share adapted material derived from this article or parts of it. The images or other third party material in this article are included in the article's Creative Commons licence, unless indicated otherwise in a credit line to the material. If material is not included in the article's Creative Commons licence and your intended use is not permitted by statutory regulation or exceeds the permitted use, you will need to obtain permission directly from the copyright holder. To view a copy of this licence, visit <http://creativecommons.org/licenses/by-nc-nd/4.0/>.

© The Author(s) 2025